

## NEUROSCIENCE

# Brain injury accelerates the onset of a reversible age-related microglial phenotype associated with inflammatory neurodegeneration

Rodney M. Ritzel<sup>1†\*</sup>, Yun Li<sup>1</sup>, Yun Jiao<sup>2</sup>, Zhuofan Lei<sup>1</sup>, Sarah J. Doran<sup>1</sup>, Junyun He<sup>1</sup>, Rami A. Shahrer<sup>1</sup>, Rebecca J. Henry<sup>1</sup>, Romeesa Khan<sup>3</sup>, Chunfeng Tan<sup>3</sup>, Shaolin Liu<sup>4</sup>, Bogdan A. Stoica<sup>1</sup>, Alan I. Faden<sup>1,5</sup>, Gregory Szeto<sup>2,6</sup>, David J. Loane<sup>1,7‡\*</sup>, Junfang Wu<sup>1,5‡\*</sup>

Lipofuscin is an autofluorescent (AF) pigment formed by lipids and misfolded proteins, which accumulates in postmitotic cells with advanced age. Here, we immunophenotyped microglia in the brain of old C57BL/6 mice (>18 months old) and demonstrate that in comparison to young mice, one-third of old microglia are AF, characterized by profound changes in lipid and iron content, phagocytic activity, and oxidative stress. Pharmacological depletion of microglia in old mice eliminated the AF microglia following repopulation and reversed microglial dysfunction. Age-related neurological deficits and neurodegeneration after traumatic brain injury (TBI) were attenuated in old mice lacking AF microglia. Furthermore, increased phagocytic activity, lysosomal burden, and lipid accumulation in microglia persisted for up to 1 year after TBI, were modified by *APOE4* genotype, and chronically driven by phagocyte-mediated oxidative stress. Thus, AF may reflect a pathological state in aging microglia associated with increased phagocytosis of neurons and myelin and inflammatory neurodegeneration that can be further accelerated by TBI.

## INTRODUCTION

Microglia have an exquisite ability to react and respond to environmental changes and stimuli to maintain neuronal homeostasis. As we age, the accumulation of a lifetime of intrinsic and extrinsic stressors gradually increases microglial dysfunction that negatively affects neurological function. Phenotypically, the changes that occur in postmitotic microglia with advanced age include increased cytokine and reactive oxygen species (ROS) production, impaired autophagic and metabolic function, and dysregulated phagocytic behavior, which may be further exaggerated in response to injury or disease (1–3). One cellular feature, lipofuscin (LF), may reflect dysfunction in all these respective pathways (4–6). LF is an autofluorescent (AF) lipopigment formed by lipids, metals, and misfolded proteins (7). Although LF granules and associated AF have long been considered a secondary consequence of the brain aging or neurodegenerative disease, there is a mounting evidence that LF may precipitate these changes and play a more active role in neurodegeneration (8).

Microglia are known to be relatively long-lived cells that show gradual turnover with limited self-renewal capacity in the aging brain (9, 10). This low rate of homeostatic cell division may prevent the dilution of LF aggregates within the aging microglial population. The buildup of LF in microglia is itself considered a marker of proliferative senescence (3, 11, 12); however, causal mechanisms have yet to be established. Microglial surveillance is vital for neuronal health and is closely linked to formation of LF through homeostatic phagocytosis of environmental debris, apoptotic cells, and excess synapses (7, 13). However, pathological phagocytosis of neurons and myelin by microglia is also associated with brain damage (14, 15), yet it is unclear whether the chronic progression of neurodegeneration and/or white matter disease caused by traumatic brain injury (TBI) are driven by pathological phagocytic activity. Whereas numerous studies have shown that LF and AF in microglia are markedly increased with normal aging (16), the functional relationship between lipid-laden microglia in age-related neurological dysfunction and brain injury has yet to be described. Here, we use flow cytometry and a simple gating strategy to identify AF microglia in the aging brain that defines hallmark phenotypic features, functional properties, and transcriptomic signatures of this unique and dysfunctional microglial population. We demonstrate that pharmacological elimination of AF microglia results in partial reversal of age-related neurological dysfunction and TBI severity. We also demonstrate that moderate-level TBI increases long-term pathological phagocytosis of myelinated neurons, accelerating lipid accumulation and associated inflammatory pathology. These features are modified by *APOE4* genotype and mediated by phagocyte-mediated oxidative stress mechanisms late after TBI.

<sup>1</sup>Department of Anesthesiology and Shock, Trauma and Anesthesiology Research (STAR) Center, University of Maryland School of Medicine, Baltimore, MD 21201, USA. <sup>2</sup>Department of Chemical, Biochemical, and Environmental Engineering, University of Maryland, Baltimore, MD 21250, USA. <sup>3</sup>Department of Neurology, McGovern Medical School, University of Texas Health Science Center at Houston, 6431 Fannin Street, Houston, TX 77370, USA. <sup>4</sup>Department of Anatomy, Howard University, Washington, DC 20059, USA. <sup>5</sup>University of Maryland Center to Advance Chronic Pain Research, University of Maryland, Baltimore, MD 21201, USA. <sup>6</sup>Allen Institute for Immunology and Department of Pediatrics, University of Washington, Seattle, WA 98109, USA. <sup>7</sup>School of Biochemistry and Immunology, Trinity Biomedical Sciences Institute, Trinity College, Dublin, Ireland.

<sup>†</sup>Present address: Department of Neurology, McGovern Medical School, University of Texas Health Science Center at Houston, 6431 Fannin Street, Houston, TX 77370, USA.

<sup>‡</sup>These authors contributed equally to this work.

\*Corresponding author. Email: rodney.m.ritzel@uth.tmc.edu (R.M.R.); loanedj@tcd.ie (D.J.L.); junfang.wu@som.umaryland.edu (J.W.)

**RESULTS****Age-related AF microglia have a unique functional phenotype associated with increased phagocytosis of neurons and myelin**

We first identified the functional phenotype of naturally occurring AF microglia (fig. S1 for gating strategy). Young adult male C57BL/6 mice (3 months old) were used as a reference to identify AF<sup>lo</sup> and AF<sup>hi</sup> microglial populations in aged 18-month-old male C57BL/6 mice by flow cytometry (Fig. 1A). Approximately one-third of microglia in aged mice were AF<sup>hi</sup> (Fig. 1, A and B). Older AF<sup>lo</sup> microglia had equivalent levels of AF as younger microglia, whereas there was a greater than ~3-fold increase in AF in old AF<sup>hi</sup> microglia (Fig. 1C). Compared to young and old bulk populations, old AF<sup>hi</sup> microglia exhibited signs of hypertrophy and increased granularity as indicated by forward and side scatter properties (fig. S2, A and B). To confirm whether AF could be attributed to LF, we examined intracellular lipid content, lipid peroxidation, and iron accumulation. Using either BODIPY 493/503 or Lipi-Blue probes to measure neutral lipids, we found that old AF<sup>hi</sup> microglia contain significantly high levels of lipid (Fig. 1D and fig. S2C). Lipid peroxidation was increased in old AF<sup>hi</sup> microglia relative to the AF<sup>lo</sup> subset as evidenced by a lower reduced/oxidized ratio (Fig. 1E), whereas iron content was higher in the old AF<sup>hi</sup> subset (Fig. 1F).

To determine whether age-related AF is associated with increases in phagocytosis, we examined several measures of phagocytic activity. Intracellular detection of endogenous neuronal marker microtubule-associated protein 2 (MAP2) in microglia revealed higher levels in old AF<sup>hi</sup> relative to AF<sup>lo</sup> (Fig. 1G). Moreover, compared to the AF<sup>lo</sup> subset, a significantly higher percentage of AF<sup>hi</sup> microglia engulfed fluorescently labeled [i.e., Thy1–green fluorescent protein (GFP) reporter] apoptotic feeder neurons by *ex vivo* assay (Fig. 1H). Intracellular detection of the myelin antigen, myelin 2',3'-cyclic nucleotide 3'-phosphodiesterase (CNPase), confirmed these findings (Fig. 1I). We validated the phagocytosis assays using neonatal microglial cultures *in vitro* in combination with immunocytochemistry (ICC) (fig. S3) and flow cytometry (fig. S4) approaches. Consistent with the increased ingestion of cargo, LC3II<sup>+</sup> autophagosome formation was significantly greater in old AF<sup>hi</sup> microglia (fig. S2D). These data are consistent with the hypothesis that age-related microglial AF is associated with LF accumulation, which is either attributable to or accelerating the engulfment of neuronal and myelin debris.

LF accumulation is cytotoxic and can potentiate inflammation and oxidative stress (7). Old AF<sup>hi</sup> microglia had higher protein expression of the phagocyte reduced form of nicotinamide adenine dinucleotide phosphate oxidase (NOX2) (Fig. 1J) and higher ROS production, as measured by dihydrorhodamine (DHR) 123 (Fig. 1K). Intracellular cytokine production of the proinflammatory mediator tumor necrosis factor (TNF) was also higher in AF<sup>hi</sup> microglia (fig. S2E), confirming the association between AF, LF, and inflammatory activity. Old AF<sup>hi</sup> microglia also had higher glucose demands, increased mitochondrial membrane potential, and lower cytosolic pH (fig. S2, F to H), which indicates that naturally occurring age-associated AF microglia have an altered metabolic profile.

**Microglial AF and its associated functional alterations are evident at middle age and driven by APOE4 genotype**

As previously reported by others (17), microglial AF increases linearly with age. We observed similar trends in postmortem human brain sections (fig. S5), in which AF Iba1<sup>+</sup> cells can also be seen in greater densities in the gray matter compared to white matter cortical regions. Qualitative analysis of gray and white matter microglia in aged mice is consistent with our findings in humans (fig. S6). These results suggest a proximal relationship between neuronal cell bodies and AF microglia, independent of age.

Middle age is seen as an axial stage in life in which biological changes can significantly alter future neurological and functional outcomes. Given that chronic inflammation in middle age can lead to cognitive problems later in life (18), and apolipoprotein E4 (APOE4) is demonstrated to be the strongest risk factor gene for Alzheimer's disease (AD) (19), we examined the contribution of APOE genotype to microglial AF and function at this stage in the life span. Young (12- to 16-week-old) and middle-aged (40- to 44-week-old) mice harboring wild-type *ApoE*, human APOE3 (hAPOE3), and hAPOE4 genotypes were evaluated. No significant differences were seen in microglia counts at young age; however, the brains of hAPOE3 and hAPOE4 mice had fewer microglia than wild-type *ApoE* mice at middle age (Fig. 2A). Unexpectedly, we found that cellular granularity and AF were significantly increased in hAPOE4 versus hAPOE3 microglia, independent of lipid levels, as measured by BODIPY stain (Fig. 2, B to D). However, we also show that hAPOE4 genotype significantly increased CD68 and lysosomal-associated membrane protein 1 (Lamp1) protein expression (Fig. 2, E and F) and production of the proinflammatory cytokine TNF (Fig. 2G) in middle-aged microglia. An engulfment assay using living SLICK-YFP (single-neuron labeling with inducible Cre-mediated knock-out–yellow fluorescent protein) neurons freshly isolated from the cortex revealed greater phagocytosis of neurons as a function of both middle-aged and APOE4 genotype (Fig. 2H). We validated the phagocytic activity of these microglia with intracellular staining for anti-YFP (Fig. 2I) and colabeling with myelin CNPase (Fig. 2J). Further experiments demonstrated that hAPOE4 genotype also modified the AF phenotype at old age (16 to 20 months old; fig. S7). Together, we found that APOE4 accelerates the development, severity, or onset of the microglial AF phenotype as early as middle age, which may have implications for the pathogenesis of neurodegenerative disease.

**Microglia depletion and repopulation reverse the age-related AF phenotype and transcriptomic signature**

LF is undegradable but can be efficiently diluted during cell division (20). Previous work demonstrated that forced microglial turnover in aged mice can reduce histological markers of LF content (21). To expand on this finding, we followed a similar microglial depletion/repopulation protocol by administering the colony-stimulating factor 1 receptor (CSF1R) antagonist, PLX5622, to 18-month-old male C57BL/6 mice in chow for 3 weeks, followed by 4 weeks of repopulation (Fig. 3, A and B). No statistically significant differences were seen in the number of brain-resident microglia in the aged brain after repopulation (Fig. 3C). PLX5622-mediated depletion and repopulation eliminated the AF<sup>hi</sup> subset in old mice, as evidenced by decreased cellular AF, granularity/size, and cytokine and ROS productions (Fig. 3D and fig. S8).

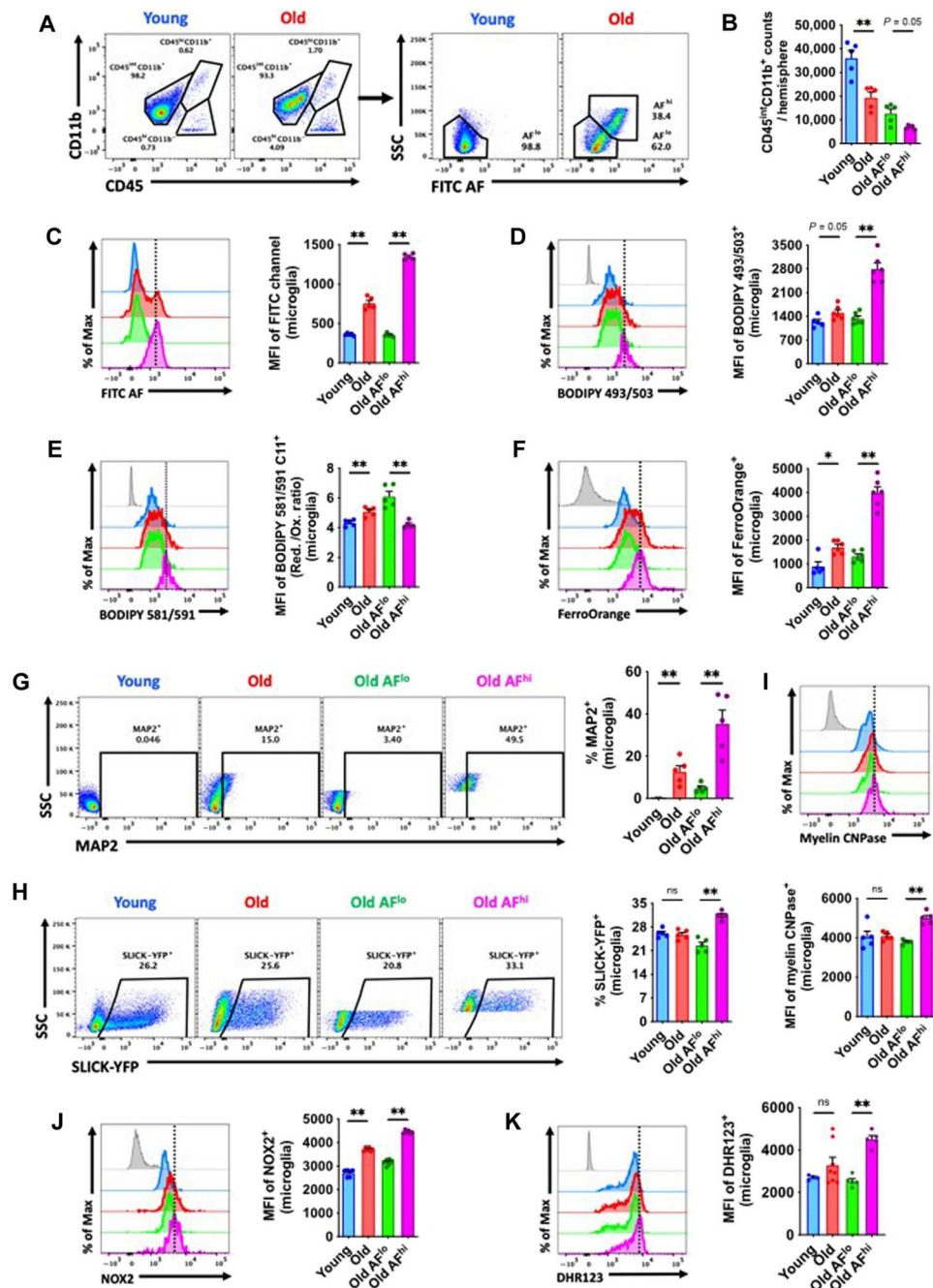


**Fig. 1. Functional characterization of age-associated AF microglia identifies a LF phenotype associated with increased phagocytic activity.** (A) Representative dot plots showing CD45<sup>int</sup>CD11b<sup>+</sup> microglia with AF low (AF<sup>lo</sup>) and AF high (AF<sup>hi</sup>) properties in young and old mice, respectively. (B) Microglia counts in young and old brain hemispheres, including for each AF subset, are shown. (C) The level of AF in each bulk microglial population and subset is quantified using the mean fluorescence intensity (MFI) of the empty fluorescein isothiocyanate (FITC) channel. Representative histograms and bar graphs are shown next to the relative MFI quantification of (D) lipid content, (E) lipid peroxidation levels, and (F) iron accumulation in microglia as demonstrated using fluorogenic dyes. Phagocytic activity was measured by (G) intracellular detection of the neuronal marker MAP2, (H) fluorescence of neuronal SLICK-YFP (single-neuron labeling with inducible Cre-mediated knockout–yellow fluorescent protein) reporter mice, and (I) intracellular detection of the myelin marker, myelin CNPase. (J and K) Oxidative stress was measured by intracellular protein expression of NOX2 and production of ROS using dihydrorhodamine (DHR) 123. *N* = 5 per group. Fluorescence minus one (FMO) controls are shown in gray, while microglial populations are color-coded according to bar graph. AF, autofluorescence; Max, maximum; Ox, oxidation; Red, reduction; SSC, side scatter; ns, not significant. Nonparametric data were analyzed using Mann-Whitney test (\**P* < 0.05 and \*\**P* < 0.01).

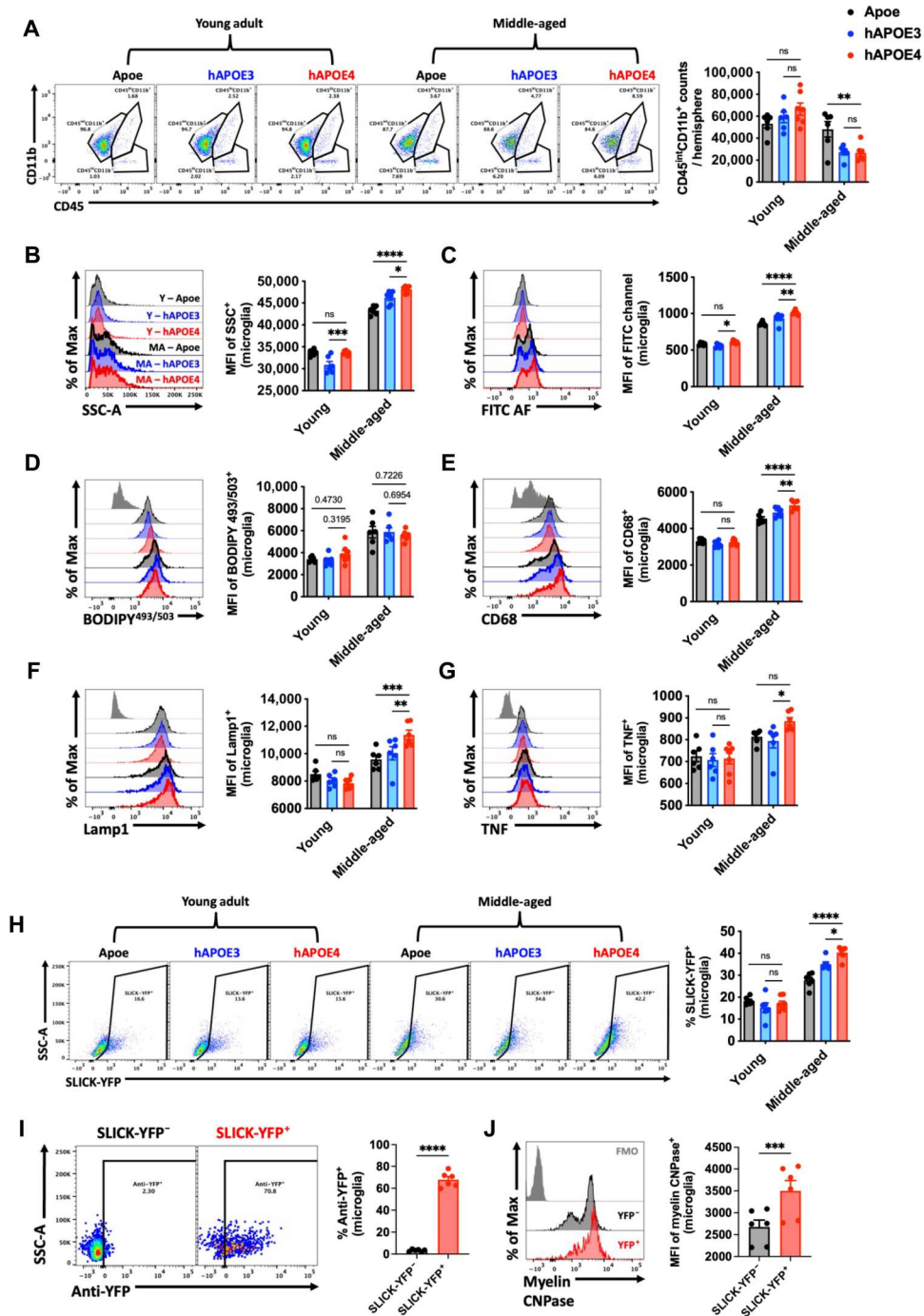


**Fig. 2. APOE4 genotype promotes the emergence of the AF phenotype at middle age.** (A) Representative dot plots show the immune profile in the brains of young and middle-aged *Apoe*, *hAPOE3*, and *hAPOE4*, quantified on the right. Representative histograms depict the relative level of cell granularity (B), autofluorescence (C), lipid accumulation (D), CD68 (E), and Lamp1 (F) protein expression and intracellular cytokine production of TNF (G) in CD45<sup>int</sup>CD11b<sup>+</sup> microglia across ages and genotypes. (H) Ex vivo neuronal engulfment assay shows a significant increase in the percent of microglia that phagocytized live Slick-YFP neurons, quantified on the right. Validation of internalized myelinated cortical neurons was performed using intracellular detection of anti-YFP (I) and anti-myelin CNPase (J) in phagocytic (Slick-YFP<sup>+</sup>) and nonphagocytic (Slick-YFP<sup>-</sup>) microglial populations within the same brain. *N* = 6 to 7 per group. MA, middle-aged; Y, young; ns, not significant. Data were analyzed using one-way analysis of variance (ANOVA) with Bonferroni post hoc correction for multiple comparisons (\**P* < 0.05, \*\**P* < 0.01, \*\*\**P* < 0.001, and \*\*\*\**P* < 0.0001).

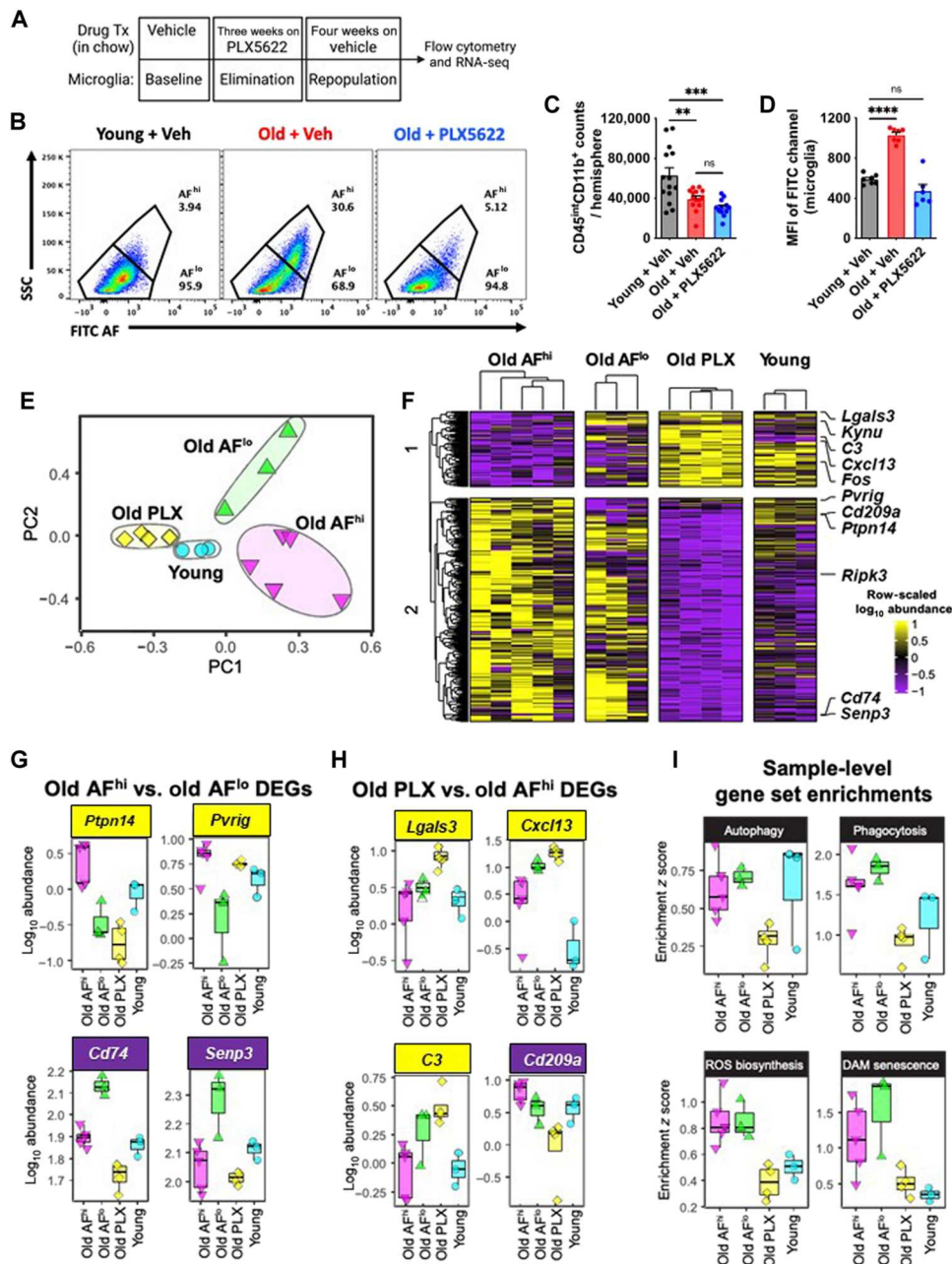


**Fig. 3. Transcriptomic signature of old, AF microglia is partially rejuvenated following elimination and 4 weeks of repopulation.** (A) Timeline of experimental design for the acute 4-week microglial repopulation period is shown. Tx, treatment. (B) A representative dot plot depicts the subsets and group conditions of FACS-sorted microglia that were evaluated downstream by RNA-seq. After 4 weeks of repopulation, the (C) number of microglia and (D) MFI in the FITC channel (i.e., relative autofluorescence) was measured. (E) PCA plot of whole transcriptomes for each microglial subset/group is shown. (F) Heatmap showing DEGs (false discovery rate < 0.1) comparing old AF<sup>hi</sup> versus old AF<sup>lo</sup>, or old PLX5622 (PLX) versus old AF<sup>hi</sup>. Expression is shown as row-scaled log<sub>10</sub> abundance. Select top-ranked DEGs from (G) old AF<sup>hi</sup> versus old AF<sup>lo</sup> and (H) old PLX5622 versus old AF<sup>hi</sup> comparisons. (I) Expression of gene sets for key functional pathways were analyzed using SLEA. Samples were z-scored on the basis of expression of selected gene sets compared to a sample-specific null distribution. ns, not significant. Data are represented from two independent experiments (N = 6 to 8 mice per group). Data (C and D) were analyzed using one-way ANOVA with Bonferroni post hoc correction for multiple comparisons (\*\*P < 0.01, \*\*\*P < 0.001, and \*\*\*\*P < 0.0001).

To characterize the transcriptomic signature of AF subsets, RNA sequencing (RNA-seq) was performed on fluorescence-activated cell sorting (FACS)-sorted microglia. Principal components analysis (PCA) on whole transcriptomes revealed that each microglial subset was distinct along the first two principal components (PCs), with old, repopulated microglia clustering closely to young microglia on PC1 and PC2 (Fig. 3E). In contrast, old microglia subsets exhibited substantially more heterogeneity as seen by their intragroup spread along both PC1 and PC2. PC2 also predominantly separated AF<sup>hi</sup> and AF<sup>lo</sup> microglia. To define the transcriptional signature of old AF<sup>hi</sup> microglia, we identified differentially expressed genes (DEGs) between old AF<sup>hi</sup> and old AF<sup>lo</sup> or old PLX5622 and old AF<sup>hi</sup> microglia. Hierarchical clustering of DEGs underscored that old PLX5622 microglia had decreased expression of a gene module associated with old AF<sup>hi</sup> and old AF<sup>lo</sup> microglia (Fig. 3F). The AF<sup>hi</sup> gene signature in old mice included up-regulation of *Pvrig*, an immune checkpoint receptor (22) and AD risk enhancer in macrophages (23), and *Ptpn14*, a potent regulator of suppressor of cytokine signaling 7 (SOCS7) (24), and down-regulation of *Cd74*, *Senp3*, and *Kynu* (Fig. 3G). A module of DEGs was also identified as up-regulated in old PLX5622 microglia, down-regulated in old AF<sup>hi</sup>, and mixed expression in young (Fig. 3H). Up-regulated genes in old PLX5622 microglia included *Cxcl13*, which is overexpressed upon microglial repopulation (25), and *C3* and *Lgals3*, which may be part of an anti-inflammatory subset of disease-associated microglia (DAM) (26). Microglial *Lgals3* has also been shown to produce anti-inflammatory and neuroprotective actions following acute ischemic injury (27) and in amyotrophic lateral sclerosis (28).

We tested whether transcriptional signatures could explain functional differences in old AF<sup>hi</sup> microglia by performing sample-level enrichment analysis (SLEA) on gene sets for phagocytosis, ROS biosynthesis, autophagy, and DAM/senescence pathways (Fig. 3I). The autophagy pathway was decreased in old PLX5622 microglia but similar in old and young microglia. Phagocytosis, ROS biosynthesis, and DAM senescence pathways were more highly expressed in old AF<sup>hi</sup> and AF<sup>low</sup> microglial populations and attenuated in old PLX5622 microglia. Gene expression for these functional pathways was not significantly different between old AF<sup>hi</sup> and old AF<sup>lo</sup> microglia. These findings not only corroborate our earlier work showing a normal age-related increase in the expression of DAM-associated genes in the brain (29) and our preceding immunophenotyping results (Fig. 1), but also suggest that some functional differences between old AF subsets are not transcriptionally regulated.

### Forced turnover of microglia in old mice restores motor function and cognitive performance

Given that depletion and repopulation of old microglia reversed several features associated with the AF phenotype and reprogrammed transcriptional networks, we next investigated whether forced microglial turnover could modify age-related neurological dysfunction using a diverse battery of behavioral tests (Fig. 4A). At 4 weeks after repopulation, significant gains in forelimb grip strength were seen in old PLX5622-treated mice (Fig. 4B, Repop group). Age-related deficits in motor coordination using a rotarod test were apparent in old mice, but there was no effect of repopulation on overall performance at either end point (Fig. 4C), consistent with earlier findings (29). Next, we evaluated gait dynamics, and microglial repopulation partially reversed age-related

deficits in regularity index, stand, stride length, and body speed parameters (Fig. 4, D to H, Repop group). There were no effects on swing speed or step cycle (fig. S9, A and B). Because cerebellar dysfunction can be an underlying cause of uncoordinated forelimb movement, we also examined the age-related cytokine milieu in the cerebellum. Significant reductions in interleukin-4 (IL-4), IL-9, IL-10, vascular endothelial growth factor, macrophage CSF (M-CSF), induced protein 10 (IP-10), macrophage inflammatory protein 1a (MIP-1a), MIP-1b, and TNF were found after microglial repopulation in old mice (fig. S10). These changes in cerebellar cytokine concentrations represented a return to young adult levels. Unexpectedly, gains in forelimb gait function persisted for up to 12 weeks after repopulation (Fig. 4, I to P) and mirrored those seen in the hindlimbs (fig. S11). Together, our data suggest that resetting the inflammatory milieu of brain regions involved in motor function can alleviate age-associated deficits in gait performance.

To better understand the longer-term benefits of forced turnover in old mice on neurological function, we examined cognitive, socialization, and depression-like behaviors at 12 weeks after repopulation (Fig. 4I). In cognitive testing, microglial repopulation in old mice increased the interaction with the novel object during the choice phase of the novel object recognition (NOR) test, indicating that forced turnover of old microglia improved declarative memory (Fig. 4Q). Age-related depression-like behaviors were also reduced following microglial repopulation in old mice as evidenced by increased mobility in both the tail suspension (TS) (Fig. 4R) and forced swim (FS) tests (Fig. 4S). Furthermore, age-related deficits in social recognition (SR), or preference for social novelty, were partially reversed in old mice with forced microglial turnover (Fig. 4T). A PCA analysis of this behavioral dataset (Fig. 4, I to T) demonstrate the stability of the rejuvenating effects that eliminating AF microglia has on neurological function (fig. S12).

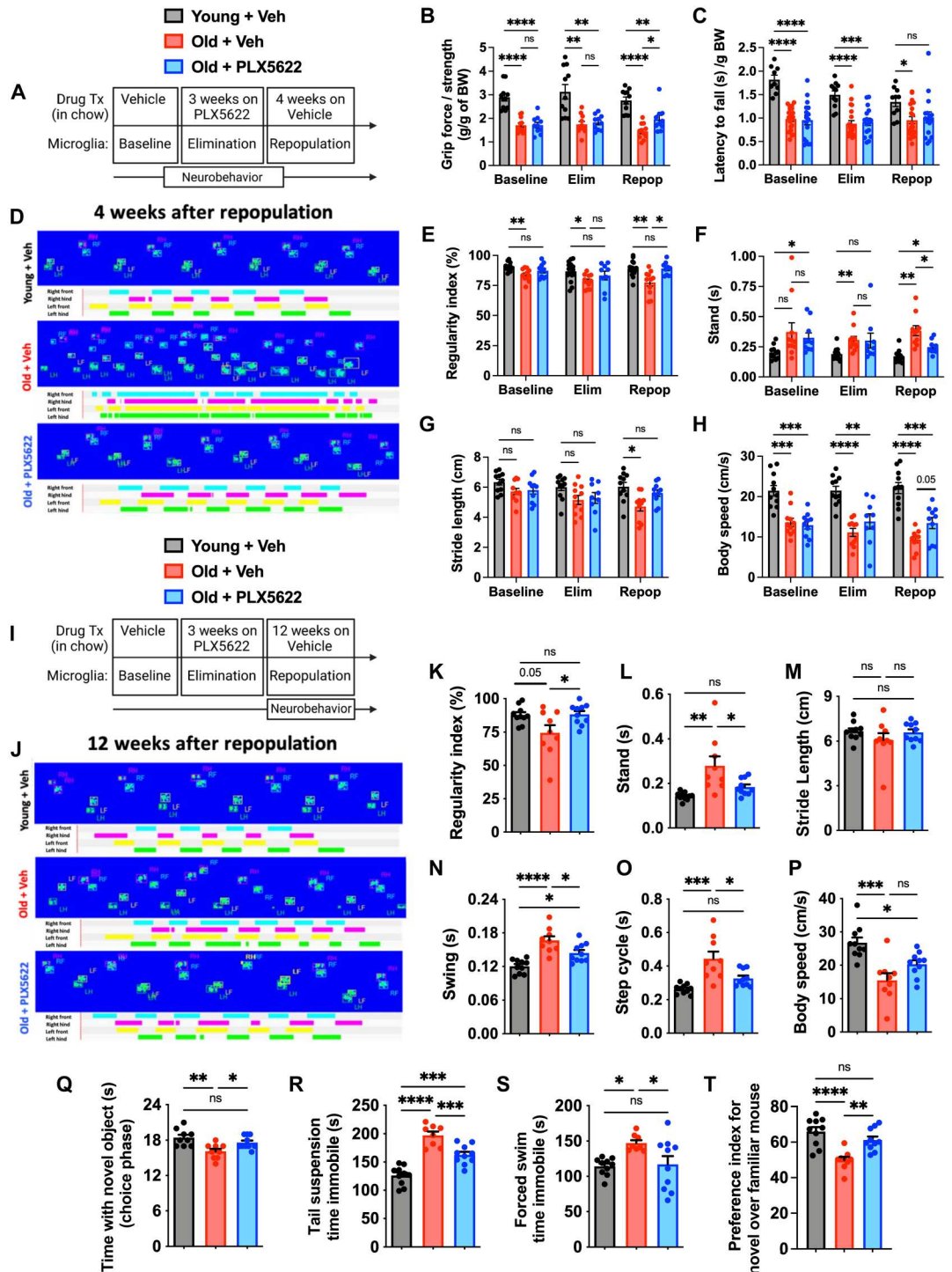
### The beneficial effects of forced turnover of AF microglia persist for months

We then investigated whether elimination of the AF<sup>hi</sup> subset was sustained late after repopulation or if the phenotype eventually re-emerges with advanced age (Fig. 5A). Age-related reductions in microglia number/yield were partially mitigated in old mice at 12 weeks after repopulation (Fig. 5B). Young and old repopulated microglia showed stable decreases in cell size and granularity compared to vehicle (Veh)-treated control groups (fig. S13, A and B, respectively). Flow cytometry measurements of AF, lipid accumulation, and iron content were each significantly attenuated at 12 weeks after repopulation, an effect only observed in aged mice (Fig. 5, C to F). A significant decrease after repopulation was also seen in microglial production of proinflammatory cytokines and ROS, as measured by 2,7-dichlorofluorescein diacetate (DCF) (Fig. 5, G to I, respectively). Consistent with this change in microglial phenotype, cellular alterations in metabolic function were also stably reversed late after forced turnover (fig. S13, C to E). These results demonstrate that the beneficial effects of forced repopulation on microglial phenotype are long-lasting.

### Old AF microglia have an exacerbated neuroinflammatory response to TBI

The improvements seen in functional measures that typically decline or become exaggerated with advanced age led us to hypothesize that elimination of AF<sup>hi</sup> microglia may have a protective effect

**Fig. 4. Forced turnover of microglia has lasting beneficial effects on neurological function in aged mice.** (A) Timeline of experimental design for the acute 4-week microglial repopulation period is shown. (B) Forelimb grip strength was quantified for each treatment phase. (C) Rotarod performance, as determined by latency to fall, is shown for each phase. (D) Representative graphical print view of the CatWalk XT automated gait analysis system at 4 weeks after repopulation. Catwalk gait analysis parameters for (E) regularity index, (F) stand, (G) stride length, and (H) body speed. (I) Timeline of experimental design for the chronic 12-week microglial repopulation period is shown. (J) Representative graphical print view at 12 weeks after repopulation. Catwalk gait analysis parameters for (K) regularity index, (L) stand, (M) stride length, (N) swing, (O) step cycle, and (P) body speed. Data were derived from combined forelimb values for all stand, stride length, swing, and step cycle parameters. (Q) Time spent interacting with a novel object during the choice phase of the novel object recognition (NOR) task at 12 weeks after repopulation is shown. Time spent immobile during (R) tail suspension (TS) and (S) forced swim (FS) tests demonstrate significant reductions in depressive-like behavior at 12 weeks after repopulation. (T) Time spent interacting with a novel mouse during sequence 3 of the SR test is shown. *N* = 10 to 11 per group (B), 11 to 21 per group (C, combined from two independent experiments), 10 to 11 per group (E to G), and 9 to 10 per group (K to T). BW, body weight; Elim, elimination; Repop, repopulation; ns, not significant. Data were analyzed using two-way ANOVA with Tukey's post hoc correction (B, C, and E to H) and one-way ANOVA with Bonferroni post hoc correction (K to T) for multiple comparisons (\**P* < 0.05, \*\**P* < 0.01, \*\*\**P* < 0.001, and \*\*\*\**P* < 0.0001).



on the aged brain's response to injury. To test this hypothesis, we subjected old mice (18 months old) to moderate-level controlled cortical impact (CCI) or sham surgery at 4 weeks following microglial repopulation (Fig. 6A). At 72 hours after injury, TBI-induced microglial proliferation and leukocyte extravasation were significantly attenuated in old repopulated mice relative to sham and Veh controls, as evidenced by lower cell counts (Fig. 6B). TBI-induced productions of ROS and IL-1 $\beta$ , including p16<sup>ink4a</sup>

protein expression, were all significantly reduced in old repopulated microglia compared to sham or injured Veh control (Fig. 6, C to E). To measure the impact of TBI on the inflammatory milieu in the perilesional cortex, we examined cytokine concentrations using multiplex enzyme-linked immunosorbent assay (ELISA). TBI caused an increase in eotaxin, monokine induced by gamma interferon (MIG), MIP-2, IL-1 $\alpha$ , granulocyte CSF (G-CSF), and M-CSF concentrations in Veh, but not PLX5622-treated TBI mice (Fig. 6F).

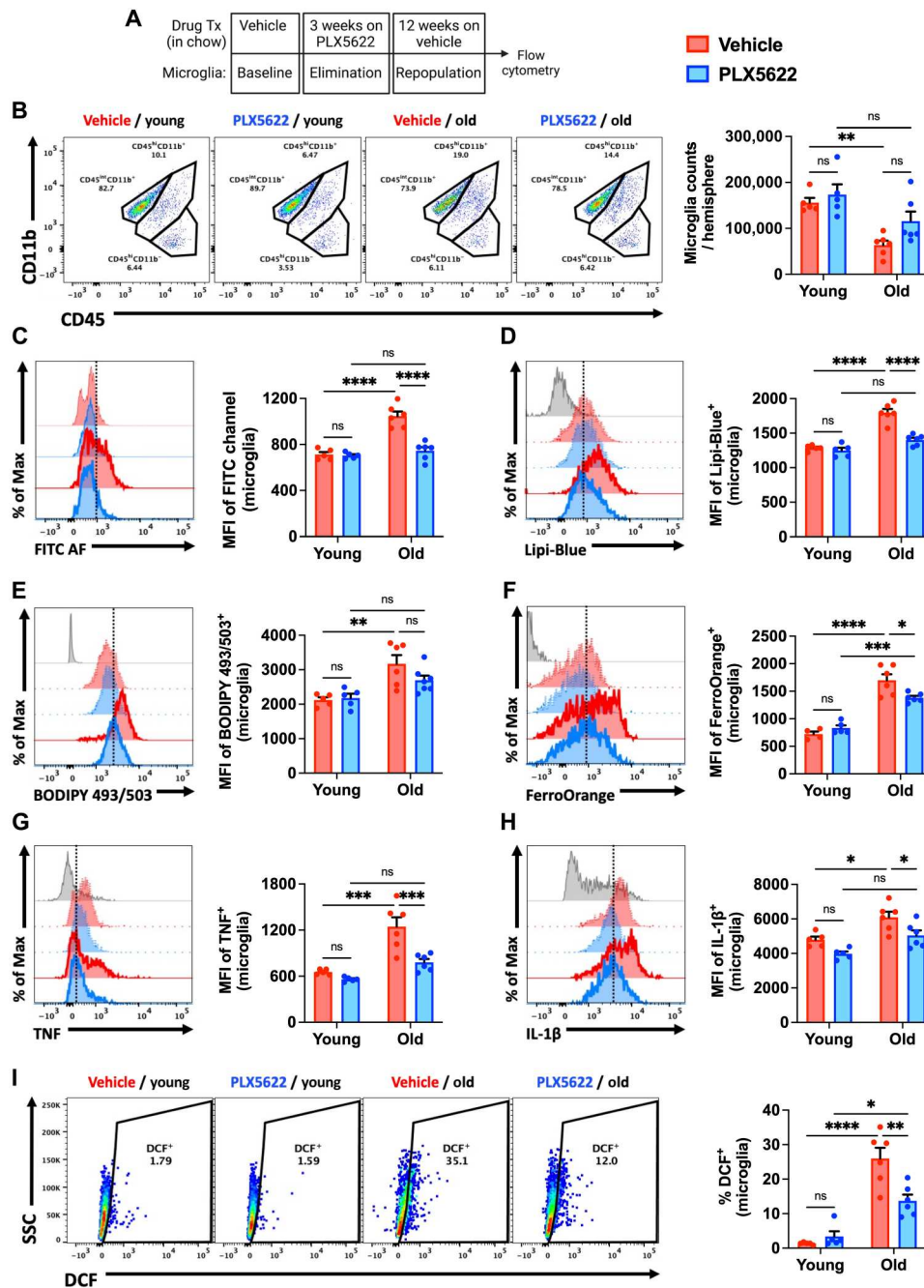
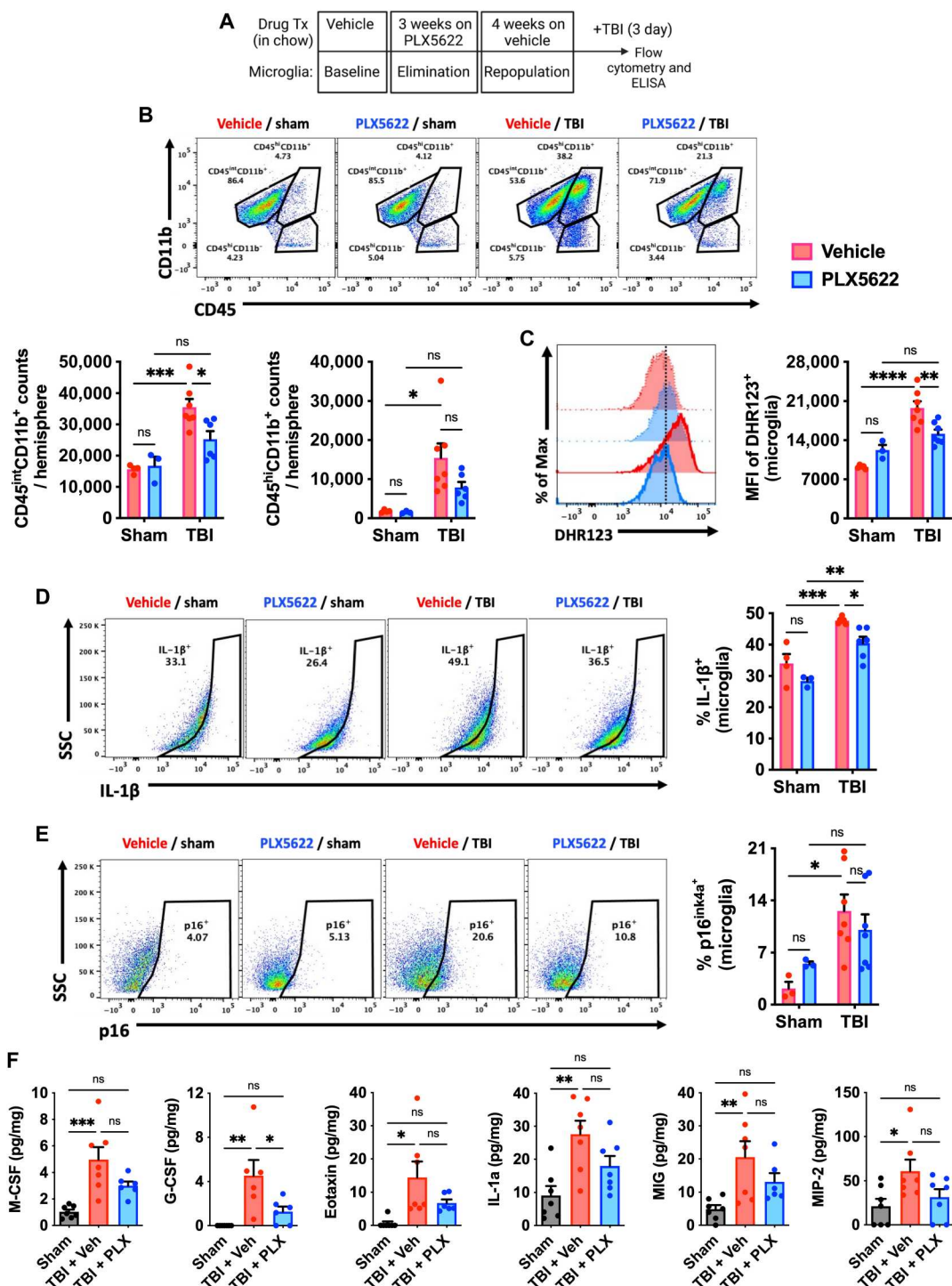


**Fig. 5. Reductions in AF-related phenotype persist for months after microglial repopulation in aged mice.** (A) Timeline of experimental design for the chronic 12-week microglial repopulation period is shown. (B) Representative dot plots of young and old microglia at 12 weeks after repopulation. Quantification of microglia counts per hemisphere is shown. Representative histograms and quantification of the AF-related phenotype as measured by MFI of (C) FITC AF, (D) and (E) lipid content, (F) iron accumulation, (G and H) proinflammatory cytokine production, and (I) ROS production. PLX5622 treatment (i.e., elimination and repopulation) showed enduring decreases in all AF-related microglial biomarkers.  $N = 4$  to 6 per group. FMO controls are shown in gray, young groups are shown with no outline, old groups are shown with bold outlines, and treatment groups are color-coded according to bar graph and figure legend (Veh in red and PLX5622 in blue). A vertical fiducial line is included for reference. ns, not significant. Data were analyzed using two-way ANOVA with Tukey post hoc correction for multiple comparisons ( $*P < 0.05$ ,  $**P < 0.01$ ,  $***P < 0.001$ , and  $****P < 0.0001$ ).

**Fig. 6. Forced turnover of microglia in aged mice decreases sensitivity to TBI.**

**(A)** Timeline of experimental design immediately before sham and TBI surgery. **(B)** Representative dot plots of immune populations in the ipsilateral brain hemisphere at 3 days after TBI. Quantification of CD45<sup>int</sup>CD11b<sup>+</sup> microglia and CD45<sup>hi</sup>CD11b<sup>+</sup>-infiltrating myeloid cell counts per hemisphere are shown for aged, surgery, and treatment groups. **(C)** A representative histogram of DHR123<sup>+</sup> microglia is shown next to the relative MFI quantification of ROS production. In the associated histogram, young groups are shown with no outline, old groups are shown with bold outlines, and treatment groups are color-coded according to bar graph and figure legend (Veh in red and PLX5622 in blue). A vertical fiducial line is included for reference. Representative dot plots depicting **(D)** IL-1 $\beta$  production and **(E)** p16 expression in microglia are shown next to quantification of cell frequencies. **(F)** Cytokine protein concentrations in the peri-lesional cortex as measured by ELISA. No differences were seen between sham control groups after treatment, and so data for both sham groups were combined. For all cytokines (M-CSF, G-CSF, eotaxin, IL-1 $\alpha$ , MIG, and MIP-2), TBI acutely increased concentrations in Veh but not PLX5622-treated groups. *N* = 3 to 4 per sham and 6 to 7 per TBI group. ns, not significant. Data were analyzed using two-way ANOVA with Tukey post hoc correction (B to E) and one-way ANOVA with Bonferroni post hoc correction (F) for multiple comparisons (\**P* < 0.05, \*\**P* < 0.01, \*\*\**P* < 0.001, and \*\*\*\**P* < 0.0001).



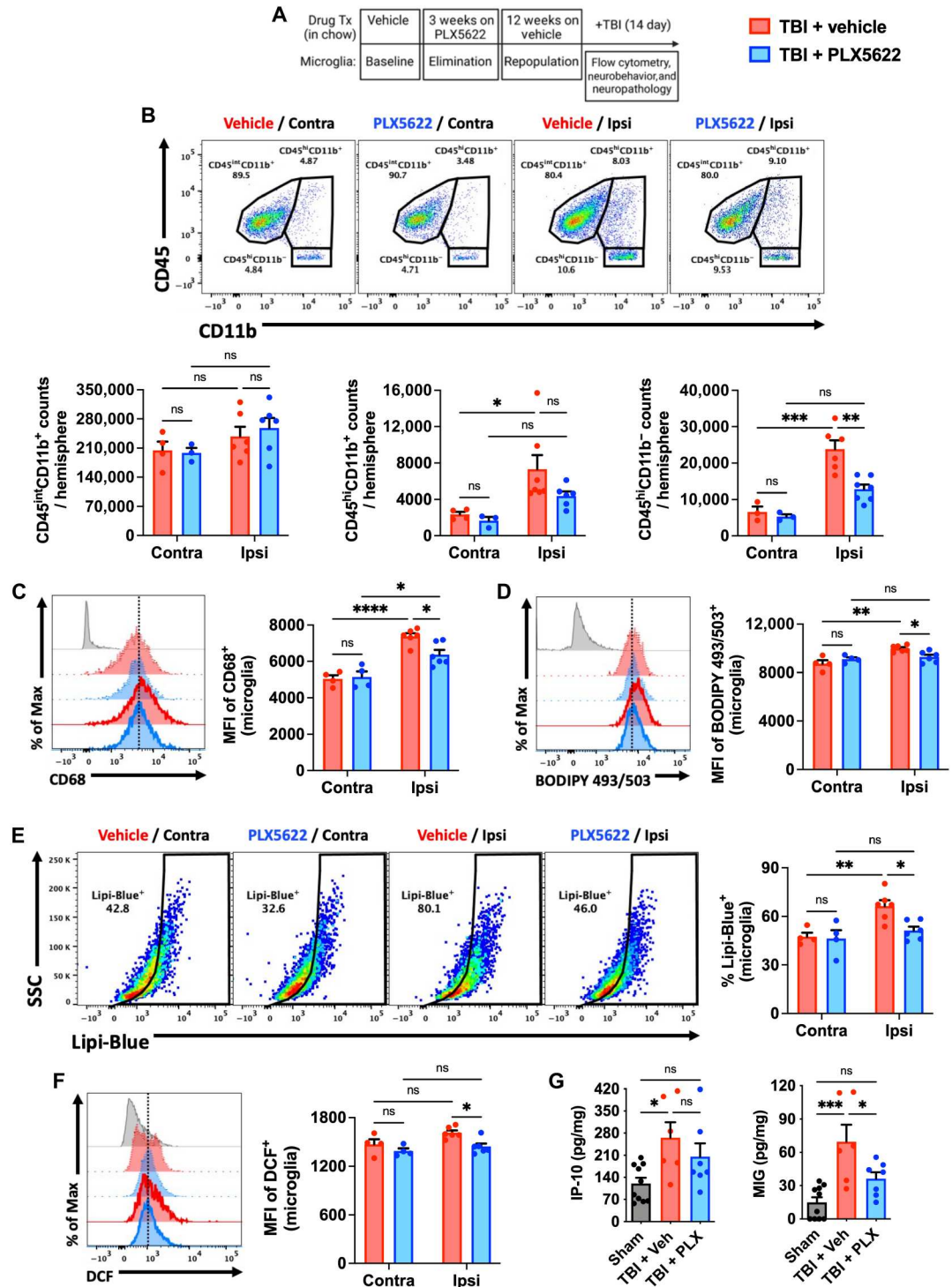
These results suggest that the presence of AF<sup>hi</sup> microglia exacerbates acute ROS and cytokine levels following TBI in old mice.

**Elimination of AF microglia in old mice reduces chronic phagocytosis and inflammatory activity following TBI**

To determine whether attenuated microglial responses to TBI were stable over time, we injured old mice (18 months old) at 12 weeks following microglial repopulation and evaluated inflammatory cell

functions at 2 weeks after injury (Fig. 7A). While the number of microglia did not differ significantly between groups after injury, the total number of CD45<sup>hi</sup> myeloid cells and lymphocytes recruited to the injured, ipsilateral hemisphere was markedly reduced in repopulated old mice (Fig. 7B). TBI-induced expression of the lysosomal marker, CD68, was attenuated in repopulated ipsilateral microglia compared to both contralateral (intact uninjured hemisphere) and injured Veh controls (Fig. 7C). Moreover, the lipid accumulation

**Fig. 7. Forced turnover of microglia in aged mice reduces chronic inflammation and emergence of the AF-related phenotype after TBI.** (A) Timeline of experimental design immediately before sham and TBI surgery. (B) Representative dot plots of immune populations in the ipsilateral and contralateral (internal control) brain hemispheres at 2 weeks after TBI. Quantification of CD45<sup>int</sup>CD11b<sup>+</sup> microglia (left), infiltrating CD45<sup>hi</sup>CD11b<sup>+</sup> myeloid (center), and CD45<sup>hi</sup>CD11b<sup>-</sup> lymphocyte (right) counts per hemisphere is shown for aged, injured, and treatment groups. (C) A representative histogram of CD68<sup>+</sup> microglia is shown next to the MFI quantification of this phagocytosis marker. (D) A representative histogram shows the relative level of neutral lipids in microglia from each hemisphere after TBI. (E) Representative dot plots depict the percentage of Lipi-Blue<sup>+</sup> microglia after TBI. The frequency of lipid droplet-containing microglia is quantified. (F) A representative histogram shows the relative level of ROS production in microglia as measured by DCF probe. (G) Cytokine protein concentrations in the peri-lesional cortex as measured by ELISA. No differences were seen between sham control groups after treatment, and so data for both sham groups were combined. *N* = 3 to 4 per contralateral and 6 to 7 per ipsilateral (i.e., TBI) group. FMO controls are shown in gray, contralateral groups are shown with bold outlines, ipsilateral groups are shown with bold outlines, and treatment groups are color-coded according to bar graph and figure legend (TBI + Veh in red and TBI + PLX5622 in blue). Contra, contralateral; Ipsi, ipsilateral; ns, not significant. Data were analyzed using two-way ANOVA with Tukey post hoc correction (B to F) and one-way ANOVA with Bonferroni post hoc correction (G) for multiple comparisons (\**P* < 0.05, \*\**P* < 0.01, \*\*\**P* < 0.001, and \*\*\*\**P* < 0.0001).



and ROS levels seen in the control group after TBI were significantly reduced in repopulated old microglia (Fig. 7, D to F). Additional staining confirmed the sustained attenuation of TBI-induced lysosomal-phagocytic functions in repopulated microglia (fig. S14). TBI caused an elevation in IP-10 and MIG tissue concentrations in the perilesional cortex that were also less pronounced in repopulated mice (Fig. 7G). These data suggested that the absence of AF<sup>hi</sup>

microglia in old mice was associated with lower levels of brain-infiltrating leukocytes and reduced lysosomal biogenesis and lipid accumulation after TBI.

## Elimination of AF microglia in old mice improves neurobehavioral outcomes and reduces chronic neurodegeneration after TBI

To validate our previous findings, we also performed neurobehavioral testing to assess functional outcomes of old mice up to 2 weeks after TBI (Fig. 7A). Compared to injured Veh control old mice, repopulated old mice also exhibited significantly better preservation of spatial working (Fig. 8A) and recognition (Fig. 8, B and C) memory in the Y-maze and NOR tests, respectively, indicating that forced turnover of AF microglia can preserve long-term cognitive function after TBI.

Next, we performed an unbiased histopathological assessment of AF microglia in the context of neurodegeneration. TBI-induced lesion volumes in old mice were significantly reduced in repopulated mice, as measured using cresyl violet (Fig. 8D). Stereological quantification of surviving neurons in the dentate gyrus region of the hippocampus revealed significantly greater preservation of neurons in the repopulated brain compared to injured Veh controls (Fig. 8E). These changes were associated with a significant reduction in Iba1<sup>+</sup> microglia/macrophages (Fig. 8, F and G) in the injured cortex of old mice. Consistent with our previous findings, we observed reduced numbers of CD68<sup>+</sup> microglia/macrophages and AF phagocytes (Fig. 8, H to L, respectively) in the repopulated brain compared to injured Veh controls. Together, these data support the notion that old AF<sup>hi</sup> microglia contribute to age-related neuropathology.

## Phagocytosis and lipid accumulation are hallmarks of posttraumatic chronic microglial activation in young mice, which is mediated by oxidative stress

Our results in old mice implied that TBI can exacerbate the AF phenotype in microglia, characterized by increased phagocytic activity and lipid accumulation. To examine this in more detail, we evaluated microglia along these phenotypic measures at chronic stages of TBI (i.e., 1 year after injury) in young C57BL/6 mice (3 months old). Microglia from chronically injured mice were significantly more likely to engulf apoptotic feeder neurons (Fig. 9A) and had significantly increased lipid content (Fig. 9B) than age-matched sham or young controls. Further analysis confirmed that microglia engulfment of neurons resulted in increased myelin uptake (Fig. 9C) and expression of CD68 (Fig. 9D). Moreover, microglia, which contained high levels of lipid, also contained high levels of iron (Fig. 9E), consistent with LF. Thus, the AF microglial immunopathological features are chronically altered after TBI.

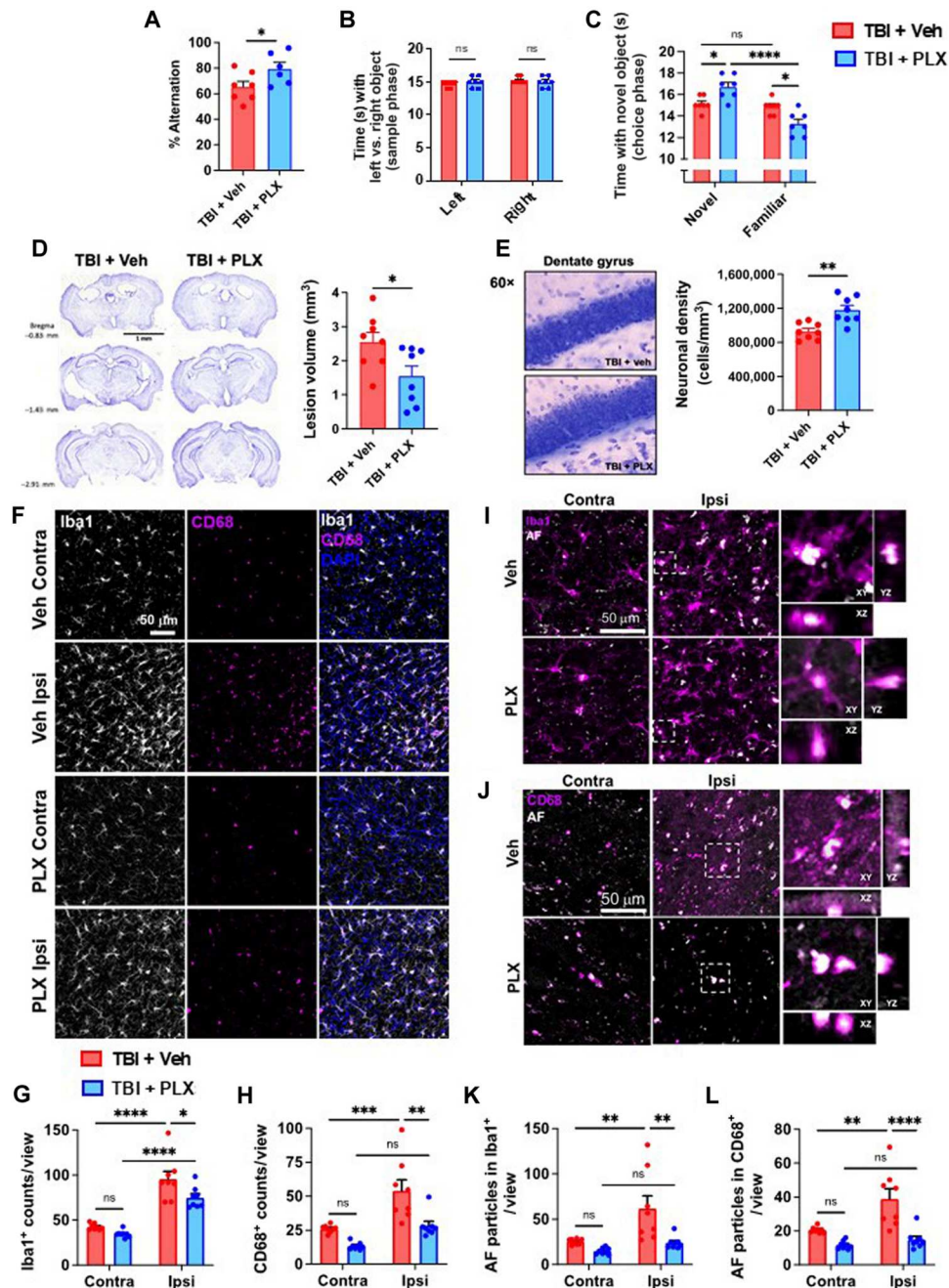
Last, we attempted to elucidate an injury-dependent mechanism through which the development of this pathological AF microglial phenotype is accelerated after TBI. Because LF is exacerbated by oxidative stress and given the close association between phagocytosis and ROS production, we used transgenic mice that have a genetic deletion of the microglial Hv1 proton channel, which is required for NOX2 activity in phagocytes (30). At 1 year after TBI, microglia from Hv1-knockout mice failed to show a chronic, injury-related increase in phagocytosis, lipid content, and oxidative stress (Fig. 10, A to D). Hv1-knockout mice had significantly better functional outcomes, including grip strength (Fig. 10E), SR (Fig. 10, F and G), and depressive-like behavior (Fig. 10H). In the NOR test, wild-type mice spent considerably less time interacting with the novel object after chronic TBI compared to Hv1-knockout mice (Fig. 10, I and J). A PCA analysis of this behavioral dataset

(Fig. 10, E to J) demonstrates the attenuation of long-term neurological deficits caused by the genetic ablation of Hv1 (fig. S15). Together, these data provide proof-of-principle evidence that phagocytic ROS intrinsically drives the emergence of the age-associated and chronic AF phenotype.

## DISCUSSION

Here, we present the first detailed immunophenotypic analysis of naturally occurring, age-associated AF microglia in the brain. This subpopulation of microglia in older mice adopt a unique dysfunctional phenotype defined by increases in phagocytosis, oxidative stress levels, lysosomal content and autophagy markers, lipid and iron accumulation, metabolic alterations, proinflammatory cytokine production, and senescent-like features. These age-associated changes in AF microglia were not regulated at the transcriptional level but were more pronounced under pathological conditions (e.g., *APOE4*) and were reversed with pharmacologically mediated cell replacement/turnover. Furthermore, we demonstrated that TBI accelerates the age of onset and tissue-wide distribution of this AF phenotype via a phagocyte-driven oxidative stress mechanism.

Our immunophenotypic characterization of age-related AF microglia converges on the recently described lipid droplet-accumulating microglia, or LDAM, which increase with age, have a proinflammatory phenotype, and are also associated with neurodegeneration (31). However, because the cellular organelles known as lipid droplets, which are involved in energy storage, were identified on the basis of neutral lipid staining, it was notable that no link was made between LDAM and LF-associated autofluorescence, which also contains neutral lipids, localizes in and around lysosomes, and increases with age and neurodegeneration. In a related study, Burns *et al.* (17) demonstrated that the AF signal in microglia increases linearly with age and is commensurate with the size and complexity of Lamp1-positive lysosomal storage bodies. Proteomic analysis of AF-positive microglia showed enrichment endolysosomal, autophagic, and metabolic pathways, including up-regulation of lysosomal degradation enzymes and proteins involved in phagosome maturation. The authors found that myelin, Fc receptor-mediated, and Triggering Receptor Expressed on Myeloid cells 2 (TREM2)-mediated phagocytosis were not dominant mechanisms contributing to AF accumulation. Rather, they found that genetic disruption of lysosomal function accelerated the accumulation of storage bodies in AF<sup>+</sup> cells and led to impaired microglia physiology and cell death. Although there is strong support for the role of lysosomal enzymes in the degradation of ingested material in neurodegenerative diseases (e.g., lysosomal storage disorders), converging transcriptomic and proteomic data also suggest that AF microglia have functional differences in phagocytic capacity highlighted by an up-regulation of biological pathways involved in the endocytosis process. However, few studies to date have demonstrated an increase in microglial phagocytosis in normal aged mice despite numerous reports of increased CD68 expression, elevated NOX2 activity, DAM-like gene signatures, and accompanying synaptic loss and myelin thinning (32). Our discovery that age-associated AF microglia exhibit a sustained increase in phagocytic activity is consistent with these features and provides a mechanistic convergence between aging and posttraumatic neurodegenerative disease.



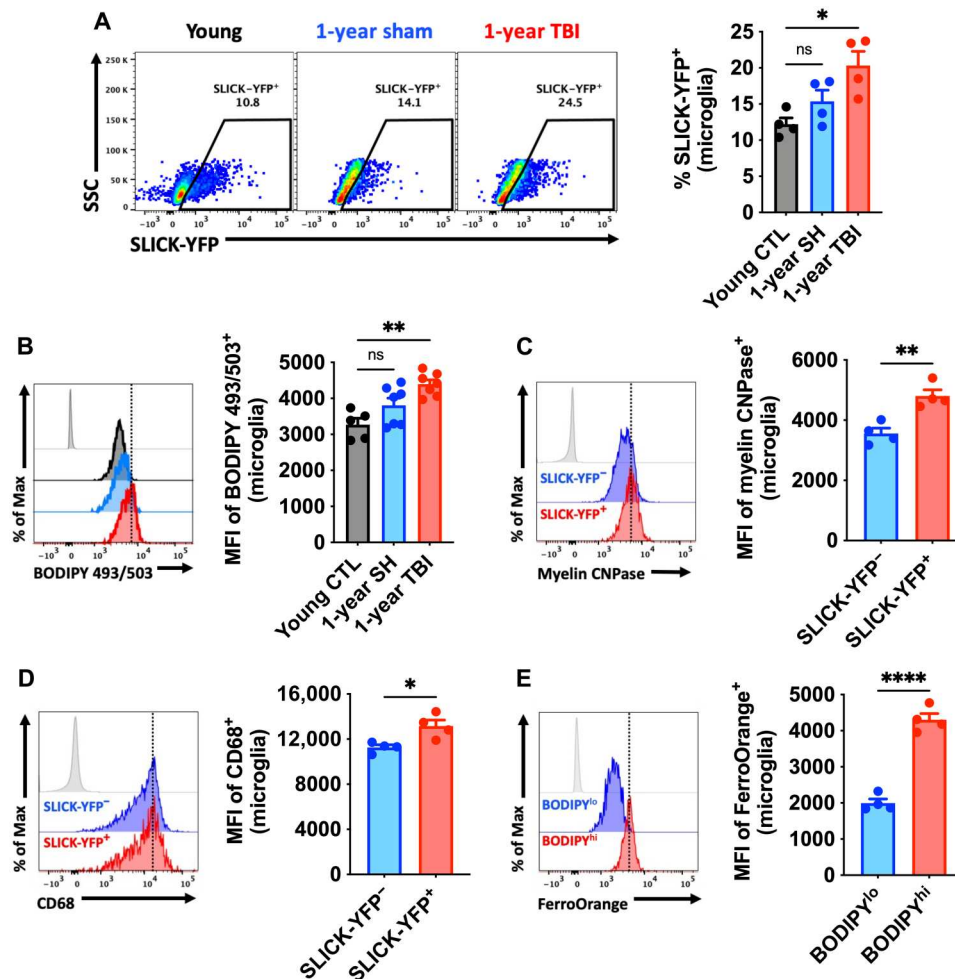


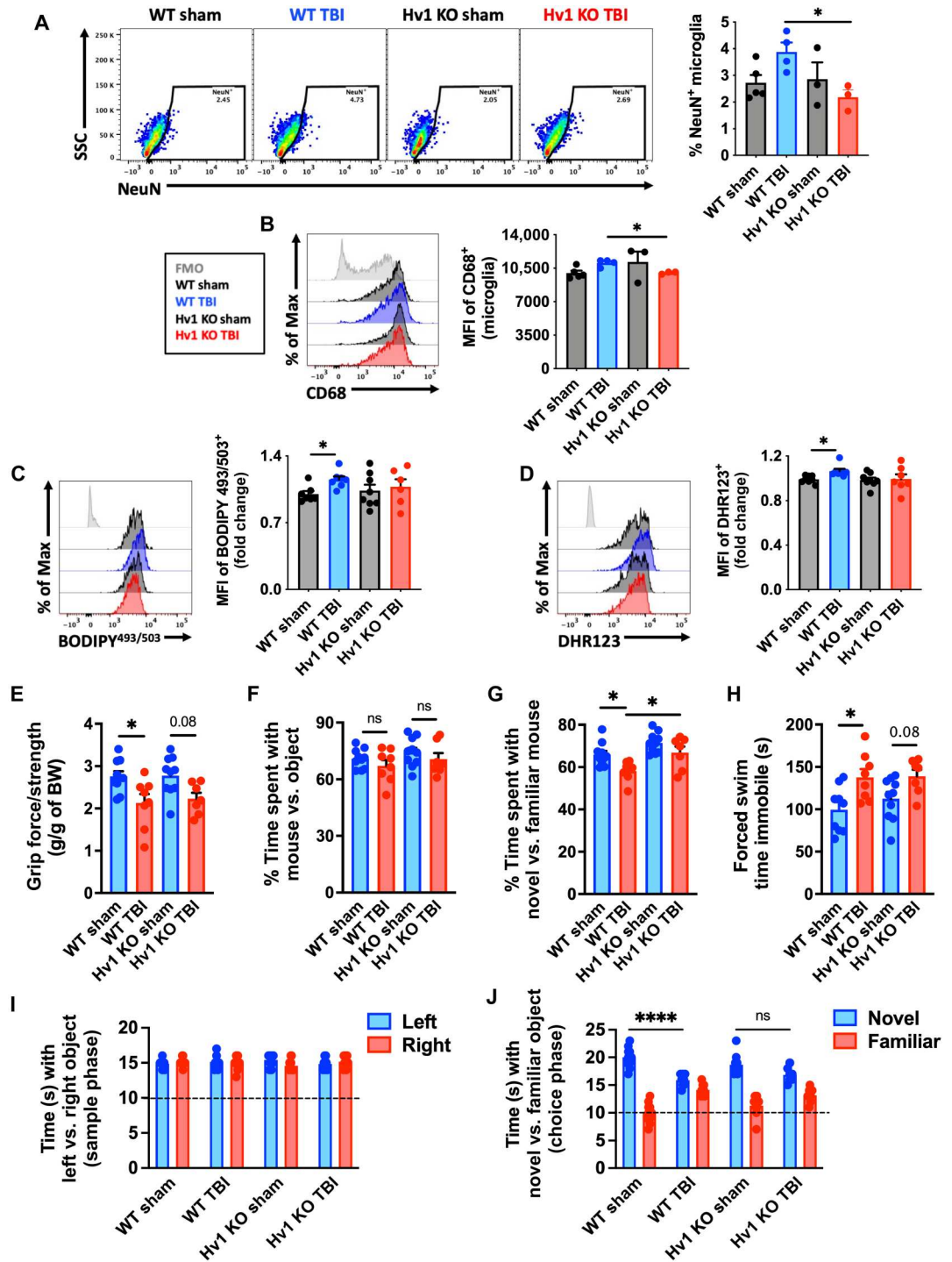
**Fig. 9. TBI accelerates development of the AF-related phenotype and chronically increases microglial phagocytosis of apoptotic neurons and myelin.** Microglial phagocytosis of neurons was assessed by ex vivo engulfment of apoptotic cortical neurons isolated from SLICK-YFP transgenic reporter mice. (A) Representative dot plots of microglia expressing YFP at 1 year after TBI. Quantification of phagocytic microglia is shown (right). (B) A representative histogram of BODIPY<sup>+</sup> microglia at 1 year after TBI is shown next to the MFI quantification of this neutral lipid marker. (C) A representative histogram shows the relative protein expression of myelin CNPase in YFP<sup>-</sup> phagocytic and nonphagocytic microglia at 1 year after TBI. (D) A representative histogram shows the relative expression level of the phagocytosis marker CD68 in YFP<sup>+</sup> and YFP<sup>-</sup> microglia. The MFI of CD68<sup>+</sup> microglia is quantified. (E) A representative histogram shows the relative level of intracellular iron deposition in subsets of microglia that are low and high in neutral lipid content at 1 year after TBI.  $N = 4$  to 7 per group. FMO controls are shown in light gray, while all other groups are shown with bold outline as color-coded according to the bar graph axis labels. A vertical fiducial line is included for reference. CTL, control; SH, sham; ns, not significant. Data were analyzed using one-way ANOVA with Bonferroni post hoc correction for multiple comparisons (A and B) and Student's  $t$  test (C to E) ( $*P < 0.05$ ,  $**P < 0.01$ , and  $****P < 0.0001$ ).

LF accumulates in postmitotic cells at a rate that occurs inversely to longevity (20). Lipid-laden neural cells can be visualized adjacent to blood vessels or deeper in the brain cortical and striatal parenchyma of aging mice and have distinct phenotypes associated with inflammation and senescence (33). Because laboratory mice live a relatively sanitary life devoid of the pathological hallmarks associated with neurodegenerative disease in humans, it was thought that LF accumulation was just a consequence of time (34). However, evidence that microglia within amyloid plaques in humans show increased LF deposition implies that this feature is pathological (35). In contrast, proliferative cells have been shown to efficiently dilute LF aggregates during cell division, showing low or no accumulation of the pigment (7). The accumulation of LF (i.e., AF phenotype) in microglia may then be indicative of replicative senescence, which

may occur naturally or following waves of injury-induced proliferation. It is reasonable to consider that microglial turnover or proliferation in aged mice may effectively dilute LF within the brain or cell population, respectively. A reversal of age-related cognitive and synaptic deficits in old mice following microglia elimination and repopulation (i.e., replacement/turnover) can be achieved using short-term treatment with the CSF1R inhibitor, PLX5622 (29). In addition, whereas microglial turnover has been demonstrated to reduce AF, partially reverse the aging microglia transcriptome (21), and improve amyloid pathology (36), several questions remain as to the linkage of these changes and which specific populations, if any, are responsible for promoting these age-related neuropathologies. Our findings suggest that AF microglia are dysfunctional, neurotoxic cells that display a senescent-like phenotype. Notably,

**Fig. 10. Hv1-driven oxidative stress promotes induction of the AF-related microglia phenotype and worsens long-term functional recovery after TBI.**

Injured  $Hv1^{-/-}$  (KO) and wild-type (WT) littermate control mice were behaviorally evaluated at 11 months after TBI, and microglia were immunophenotyped at 12 months. (A) A representative dot plot of microglia containing NeuN antigen at 1 year after TBI in WT and  $Hv1$  KO mice. Quantification of phagocytic microglia is shown (right). (B) A representative histogram shows the relative expression level of the lysosomal marker CD68 in microglia. The MFI of CD68-positive microglia is quantified (right). (C) The relative level of neutral lipids in microglia is shown at 1 year after TBI. The MFI of BODIPY<sup>+</sup> microglia is quantified (right). (D) A representative histogram shows the relative level ROS production in microglia and MFI quantification of DHR123<sup>+</sup> microglia is shown (right). (E) Forelimb grip strength was significantly reduced in WT but not  $Hv1$  KO mice after TBI. (F) The percent of time spent interacting with a mouse versus object, and (G) time spent interacting with a novel stranger mouse versus familiar mouse in the SR test. (H) Time spent immobile during the FS test is shown for all groups. (I) The time spent interacting with left versus right objects during the sample phase and (J) the time spent interacting with a novel versus familiar object during the choice phase of the object recognition test.  $N = 3$  to 5 per group (A and B) and 7 to 10 per group (C to J). ns, not significant. Data were analyzed using one-way ANOVA (A to D and E to H) and two-way ANOVA (I and J) with Bonferroni post hoc correction for multiple comparisons (\* $P < 0.05$  and \*\*\*\* $P < 0.0001$ ).



pharmacological depletion of microglia in aged mice effectively eliminated the AF population, partially restoring cellular and neurological functions.

The particular source of microglial LF during aging and chronic injury is not entirely clear. One intriguing possibility is that LF-containing neurons are phagocytosed by microglia. In this scenario, the indigestible AF material would be transferred from one cell type to another but would likely remain undigested and exacerbate the

inflammatory activation or senescent-like profile of the host microglia. To this end, our human brain analyses revealed large numbers of AF cells with neuronal morphology in the cortex of older subjects, which was not obvious in aged mice. The functional state of aging postmitotic neurons containing AF is not well understood outside of studies on lysosomal storage diseases but deserves wider attention.

We observed that AF levels and lysosomal burden were more regularly associated with increases in cell granularity (i.e., side scatter) than cell size (i.e., forward scatter). Thus, amoeboid or hypertrophic microglial morphologies may indicate a pre-AF<sup>hi</sup> state. LF accumulation may be a driving factor for, or a consequence of, the increased phagocytosis of neurons and myelin. One might surmise that LF burden, arising from defective autophagy, may induce an exhausted state that limits endocytic processes rather than an actively surveilling, phagocytic state. However, these changes are in line with the gene networks activated in microglia in AD and other neurodegenerative conditions, where increases in microglial LF/AF have also been demonstrated (7, 8). Our findings appear to confirm the existence of a DAM-like gene signature, validated at the protein and functional level, in a subset of brain microglia found in normal aged mice. The finding that TBI accelerates this complex phenotype lends further credence to the notion of brain injury-induced immune senescence. While TBI itself is a risk factor for AD, it remains to be seen whether the emergence of DAM genes involved in autophagy, lipid metabolism, and phagocytosis in AD are spurred on by an increased conversion of microglia to an AF phenotype.

Age-associated mechanisms of the composite AF phenotype are lacking. The  $\epsilon 4$  allele of the *APOE* gene is a genetic risk factor for atherosclerosis, stroke, and dementia (37) and is primarily expressed by astrocytes and microglia within the brain (38). These cells have since been shown to play key roles in secondary neurodegeneration after TBI and in the pathogenesis of AD. Recent work using human inhibitory postsynaptic currents carrying *APOE3* and *APOE4* genotypes suggests that lipid imbalances can impair essential processes in differentiated astrocytes and microglia (39). Given its role in lipid transport and metabolism, we were surprised that middle-aged h*APOE4* microglia did not exhibit elevated lipid levels compared to h*APOE3* microglia. However, our assessment was limited to neutral lipids and did not consider other lipid types. Regardless, all other aspects of the AF phenotype were exacerbated in h*APOE4* microglia at middle age, including increased phagocytosis of living cortical neurons and myelin. Thus, our findings demonstrate that older microglia exhibit greater engulfment of not only apoptotic neurons but otherwise living, healthy neurons too. These data provide a potential link between *APOE* and pathological phagocytic behavior such as impaired clearance of protein aggregates or dysregulated synaptic loss and white matter degradation in older age.

The present study also demonstrated the close association of AF microglia with neuroinflammation, neurodegeneration, and neurological decline in aged mice. To date, there is no method available to selectively deplete LF/AF microglia that would support causality. However, our finding that AF microglia have a neurotoxic phenotype that can promote cytokine-mediated tissue inflammation, leukocyte recruitment, hippocampal neuron loss, and functional decline provides a plausible explanation for age-related inflammatory-driven neuropathologies in animals. Moreover, because falls at ground level are the leading cause of TBI in older individuals (40) and forced microglial turnover ameliorated gait deficits, the presence or abundance of AF microglia may not only worsen outcome but also increase risk.

Our finding that moderate-to-severe TBI at young maturity or old age can promote and intensify the emergence of microglial AF is consistent with the notion of accelerated immune aging and

suggests an inducible and shared phenotype that exists along a continuum of neurodegenerative disease risk or severity. Sustained increases in expression of the lysosomal marker CD68 and positive regulator of phagocytosis, NOX2, have previously been shown in chronically injured mice as late as 1 year after TBI (41). Moreover, microglial phagocytosis of both living and apoptotic neurons and synapses was evident for up to 8 months after TBI, coincident with decreased synaptic protein expression in neurons (42). An age-related increase in chronic engulfment of neuronal and myelin antigens late after TBI has also been demonstrated, and these changes were accompanied by an age-related increase in the tissue expression of DAM genes, microglial ROS production, white matter loss, and hippocampal neuron death (43). Thus, the AF phenotype may identify a subset of dysfunctional or neurotoxic microglia responsible for these molecular signatures within heterogeneous cell and tissue samples. While up-regulation of the *c-Fos* gene seen in our bulk cell RNA-seq data may indicate that cell damage occurred during the isolation procedure (44), there is no clear evidence that DAM networks or senescence pathways are composed of fast response genes, suggesting that these are stable biomarkers associated with the AF phenotype. Moreover, we have validated these transcriptional pathways at the functional and protein level. A direct comparison between AF microglia from normal aged, chronic TBI, and other neurodegenerative disease states is required to better understand the homology of phenotypic features and inflammatory signatures. However, because these studies may be fraught with confounding factors of age, genotype, comorbidities, and disease staging, careful consideration is needed.

The observation that oxidative stress mediates autophagic dysregulation and formation of LF with advanced age is rationale and supported in the literature. ROS have been demonstrated to contribute to LF buildup and proinflammatory activation in neural cells, peripheral macrophages, and microglia (5, 20, 45–48). That a similar phenomenon occurs after brain injury is not well documented despite evidence for persistent basal elevation of NOX2, ROS production, oxidative stress, autophagic dysregulation, loss of proteostasis, and proinflammatory phenotype (49–52). NOX2-deficient mice exhibit acute neuroprotection and fewer neurological deficits after TBI (53, 54). Experimental manipulation of ROS production, the oxidative stress response, and autophagy have likewise been demonstrated to attenuate neuroinflammation, neuronal loss, and functional impairment. AF<sup>hi</sup> microglia produced higher levels of NOX2 and ROS, but whether it was the cause or consequence of LF was not clear. Using mice deficient in Hv1, a proton channel present on phagosomes that facilitates sustained NOX2-mediated ROS production in phagocytes, we had previously showed that neuroinflammation and neurodegeneration were significantly reduced after TBI (55). Here, we show that Hv1 chronically drives oxidative stress in phagocytes, promotes engulfment of neuronal debris, increases LF, and worsens neurological outcome. It is possible that *APOE4* genotype and oxidative stress work synergistically to augment the age-related injury AF phenotype, but further investigation is required.

In summary, our data suggest that AF reflects a pathological state in aging microglia associated with phagocytosis and inflammatory neurodegeneration that can be further accelerated by TBI. This newly immunophenotypically defined AF microglial population may serve as a useful imaging biomarker of DAM/senescence that may be otherwise underrepresented or difficult to detect in whole

tissue or bulk cell molecular analyses given its largely posttranscriptional/translational underpinnings. Mechanistically, *APOE4* genotype at middle and old age and chronic injury-induced oxidative stress promote the AF phenotype. Last, pharmacological intervention can eliminate the AF microglial signature, reduce inflammatory burden, improve neurological function, and prophylactically protect the brain against severe head impact.

## MATERIALS AND METHODS

### Animals

Young adult (3 months old) and aged (18 months old) male C57BL/6 mice bred in-house from Charles River Laboratories were housed on sawdust bedding in a specific pathogen-free facility (12-hour light/dark cycle). B6(SJL)-*Apoe*<sup>tm1.1(APOE\*4)A<sup>diuj</sup>/J</sup> (stock no. 027894) and B6.Cg-*Apoe*<sup>em2(APOE\*)A<sup>diuj</sup>/J</sup> (stock no. 029018), homozygous for a h*Apoe4* or h*Apoe3* gene targeted replacement of the endogenous mouse *Apoe* gene, were obtained from the Jackson Laboratories. Homozygous Hv1 mice breeders were obtained from L. J. Wu's laboratory at Mayo Clinic, Rochester, MN and maintained in the University of Maryland School of Medicine at Baltimore animal facility. SLICK-A transgenic mice [the Jackson Laboratories, B6.Cg-Tg(Thy1-cre/ERT2,-EYFP)AGfng/J; stock no. 007606] were used for phagocytosis studies as previously described (42). All animals had access to chow and water ad libitum. Animal procedures were performed in accordance with National Institutes of Health (NIH) guidelines for the care and use of laboratory animals and approved by the Animal Care Committee of the University of Maryland School of Medicine.

### PLX5622 administration

PLX5622 was provided by Plexikon and formulated in AIN-76A rodent chow by Research Diets at a concentration of 1200 parts per million (56, 57). Standard AIN-76A diet was provided as Veh control. Mice were provided ad libitum access to PLX5622 or Veh diet for 3 weeks to deplete microglia. After 3 weeks of depletion, mice were placed back on normal chow for either 4 or 12 weeks to allow for repopulation. The dose and time resulted in depletion of 95% of microglia and significant depletion of CD115/CSF1R-expressing myeloid cells in other peripheral organs consistent with previous studies (fig. S16) (58).

### Controlled cortical impact

Our custom-designed CCI injury device consists of a microprocessor-controlled pneumatic impactor with a 3.5-mm-diameter tip, as previously described (42, 55). Briefly, mice were anesthetized with isoflurane evaporated in a gas mixture containing 70% N<sub>2</sub>O and 30% O<sub>2</sub> and administered through a nose mask. Mice were placed on a heated pad, and core body temperature was maintained at 37°C. The head was mounted in a stereotaxic frame, a 10-mm midline incision was made over the skull, and the skin and fascia were reflected. A 5-mm craniotomy was made on the central aspect of the left parietal bone. The impounder tip of the injury device was then extended to its full stroke distance (44 mm), positioned to the surface of the exposed dura, and reset to affect the cortical surface. Moderate-level CCI was induced using an impactor velocity of 6 m/s, a deformation depth of 1 mm, and a dwell time of 50 ms (43). After injury, the incision was closed with interrupted 6-0 silk sutures, anesthesia was terminated, and the animal was

placed into a heated cage to maintain normal core temperature for 45 min after injury. Sham animals underwent the same procedure as CCI mice except for craniotomy and cortical impact. In the 14d and Hv1 TBI cohorts, an injury of moderate severity was induced by a TBI-0310 Head Impactor (Precision Systems and Instrumentation) with a 3.5-mm-diameter tip, followed by impact velocity of 4.3 m/s and a displacement depth of 1.2 mm (43).

### Flow cytometry and ex vivo functional assays

Following transcardial perfusion with 40 ml of ice-cold sterile phosphate-buffered saline (PBS), the intact brain was harvested, and the ipsilateral hemisphere isolated by removing the olfactory bulbs and cerebellum. Brain hemispheres were mechanically digested using a razor blade to mince tissue and were passed through a 70- $\mu$ m filter using RPMI 1640. Central nervous system tissue was then enzymatically digested using deoxyribonuclease (10 mg/ml; Roche), collagenase/dispase (1 mg/ml; Roche), and papain (25 U; Worthington Biochemical) for 1 hour at 37°C in a shaking CO<sub>2</sub> incubator (200 rpm). Tissue homogenates were centrifuged at 1500 rpm for 5 min at 4°C. The supernatant was discarded, and the cells were resuspended in 70% Percoll (GE Healthcare) and underlaid in 30% Percoll. This gradient was centrifuged at 500g for 20 min at 21°C. Myelin was removed by suction, and cells at the interface were collected. Leukocytes were washed and blocked with mouse Fc block (eBioscience, clone 93) before staining with primary antibody-conjugated fluorophores CD45-eF450 (30-F11), CD11b-APCeF780 (M1/70), Ly6C-allophycocyanin (APC) (HK1.4), and Ly6G-phycoerythrin (PE) (1A8) were purchased from eBioscience, whereas CD45-PerCP-Cy5.5 (30-F11) and CD11b-PerCP-Cy5.5 (M1/70) were purchased from BioLegend. For live/dead cell discrimination, a fixable viability dye, Zombie Aqua (BioLegend), was dissolved in dimethyl sulfoxide according to the manufacturer's instructions and added to cells in a final concentration of 1:50. Data were acquired on an LSRII using FACSDiva 6.0 (BD Biosciences) and analyzed using FlowJo (Tree Star). A standardized gating strategy was used to identify microglia (CD45<sup>int</sup>CD11b<sup>+</sup>Ly6C<sup>-</sup>) and brain-infiltrating myeloid cells (CD45<sup>hi</sup>CD11b<sup>+</sup>), including monocyte (CD45<sup>hi</sup>CD11b<sup>+</sup>Ly6C<sup>+</sup>Ly6G<sup>-</sup>) and neutrophil (CD45<sup>hi</sup>CD11b<sup>+</sup>Ly6C<sup>+</sup>Ly6G<sup>+</sup>) populations, as previously described (59). Cells were also stained with the surface markers CD115 (CSF1R)-Alexa Fluor 488 (BioLegend, AFS98), CD16/32-APC (BioLegend, 93), and CD369 (CLEC7A)-APC (BioLegend, RH1). Cell-specific fluorescence minus one (FMO) controls were used to determine the positivity of each antibody. To control for normal age-related autofluorescence, FMO controls were generated by combining young and aged brain samples or aged brain samples alone. Microglial AF subsets were delineated using young and aged microglia for each experiment as described by others (17), with minor modification. Cell count estimations were performed using CountBright absolute counting beads (20  $\mu$ l per test; Invitrogen, Carlsbad, CA, USA) according to the manufacturer's instructions.

Intracellular staining was performed using a fixation/permeabilization kit (BD Biosciences) and the following antibodies: p16<sup>ink4a</sup>-APC (StressMarq Biosciences, SPC-1280D), NOX2-Alexa Fluor 647 (Bioss Antibodies, bs-3889R), glyceraldehyde-3-phosphate dehydrogenase-Alexa Fluor 488 (BioLegend, W17079A), Lamp1-PerCP-Cy5.5 (BioLegend, 1D4B), Lamp2-PE (BioLegend, M3/84), NeuN-PE (MilliporeSigma, A60), MAP2-Alexa Fluor 594

(BioLegend, SMI 52), myelin CNPase-Alexa Fluor 647 (BioLegend, SMI 91), anti-GFP-PE (BioLegend, FM264G), and CD68-PE-Cy7 (BioLegend, FA-11).

For intracellular cytokine staining, leukocytes were collected as described above, and 1  $\mu$ l of GolgiPlug containing brefeldin A (BD Biosciences) was added to 500  $\mu$ l of complete RPMI 1640. Cells were then resuspended in Fc block, stained for surface antigens, and washed in 100  $\mu$ l of fixation/permeabilization solution (BD Biosciences) for 20 min. Cells were washed twice in 500  $\mu$ l of permeabilization/wash buffer (BD Biosciences) and resuspended in an intracellular antibody cocktail containing cytokine antibodies [MMP-9-R-PE (StressMarq Biosciences, SMC-396D), TNF-PE-Cy7 (eBioscience, MP6-XT22), IL-1 $\alpha$ -PE (BioLegend, ALF-161), and IL-1 $\beta$ -PerCP-eF710 (eBioscience, NJTEN3) and fixed.

For ROS detection, leukocytes were incubated with DHR 123 (5 mM; Life Technologies/Invitrogen) or 2',7'-dichlorodihydrofluorescein diacetate (DCF, 5  $\mu$ M; Thermo Fisher Scientific), cell-permeable fluorogenic probes. Cells were loaded for 20 min at 37°C, washed three times with FACS buffer (without NaAz), and then stained for surface markers including viability stain. Lipid peroxidation was measured using BODIPY 581/591 C11<sup>+</sup> (Invitrogen). LC3-associated autophagic vesicles were measured using the CYTO-ID autophagy detection kit (Enzo Life Sciences) according to the manufacturer's instructions. Lysosomes were labeled using LysoTracker Green DND-26 (Invitrogen). Intracellular myelin content was stained with FluoroMyelin Red (Invitrogen). Neutral lipids and lipid droplets were measured using BODIPY 493/503 (Invitrogen) and Lipi-Blue (Dojindo, LD01-10). Intracellular iron levels were measured using FerroOrange (Dojindo). Relative intracellular pH was measured using Protonex Red 600 (5  $\mu$ M; AAT Bioquest). Mitochondrial membrane potential was measured using MitoSpy Red dye (BioLegend) according to the company's protocol. Glucose uptake was measured using 2-[N-(7-Nitrobenz-2-oxa-1,3-diazol-4-yl)Amino]-2-Deoxyglucose (2NBD)-glucose uptake cell-based assay kit (Cayman Chemical).

Microglial phagocytosis of apoptotic neurons was performed as described by Ritzel *et al.* (42). Briefly, YFP-positive neurons were isolated from the cortices of an adult SLICK transgenic mouse and then exposed to heat shock for 5 min at 60°C, washed in Hanks' balanced salt solution (HBSS), resuspended in 5 ml of RPMI 1640, and kept on ice. Soon after, 50  $\mu$ l of feeder YFP-positive cells were incubated with freshly isolated microglia for 45 min at 37°C. For assays using live feeder neurons, apoptosis was not induced. Afterward, the cells were washed three times with 1 ml of PBS, stained and fixed as above, and collected on the cytometer.

### FACS of microglia

Living CD45<sup>+</sup>CD11b<sup>+</sup>Ly6C<sup>-</sup> microglia were sorted (100- $\mu$ m nozzle/18 psi) using an FACS Aria II (BD Biosciences) by the University of Maryland Greenebaum Comprehensive Cancer Center Flow Cytometry Shared Service Core. Before sorting, brain hemispheres were processed as above using FACS buffer without sodium azide or fixation. Brain leukocytes were washed and blocked with mouse Fc block (Thermo Fisher Scientific, clone 93) before staining with primary antibody-conjugated fluorophores. CD45-eF450 (30-F11), CD11b-APCeF780 (M1/70), and Ly6C-APC (HK1.4) were purchased from Thermo Fisher Scientific. For live/dead cell discrimination, the viability dye, 7-aminoactinomycin D (7-AAD) (BioLegend), was diluted at 5  $\mu$ l in 100- $\mu$ l sample. Data

were acquired, and microglia were sorted by flow cytometry on an FACS Aria II using FACSDiva 6.0 (BD Biosciences). Purified microglia from individual hemispheres were collected in 300  $\mu$ l of RNAProtect cell reagent (QIAGEN) with  $\beta$ -mercaptoethanol (Sigma-Aldrich) into a standard sterile 1.5 ml of ribonuclease-free Eppendorf microcentrifuge tube, vortexed for 30 s, snap-frozen in dry ice, and then stored in -80°C until RNA extraction. Each tube was later thawed, vortexed again, and poured over a column using the RNA kit as described. All microglia were sorted on two separate days within the same week using the same materials and reagents. On the first sort day, young bulk (i.e., AF<sup>lo</sup>), old AF<sup>lo</sup>, and old AF<sup>hi</sup> microglia populations were collected ( $n = 4$  per group). Microglial AF levels were quantified for each FACS-sorted group (fig. S8). On the second day, young + Veh, old + Veh, and old + PLX5622 (i.e., 3 weeks elimination + 4 weeks repopulation) bulk microglia populations were collected ( $N = 4$  per group). Approximately 5000 to 55,000 microglia were collected for each tube per group.

### RNA-seq and transcriptomic analysis

FACS-sorted microglia cells were flash frozen in dry ice into 300  $\mu$ l of RNAProtect cell reagent (QIAGEN). Total RNA was extracted using RNeasy mini kit (QIAGEN). RNA samples were sent to the Institute for Genome Sciences at University of Maryland School of Medicine for RNA quality test and RNA-seq. The RNA quality was analyzed using low-input Pico chip on Agilent 2100 Bioanalyzer. Amplification of cDNA from the total RNA samples were performed using Ovation RNA-seq system kit (Tecan), followed by low input RNA-seq library preparation. RNA-seq of all libraries was performed on Illumina HiSeq4000. The data were converted to FastQ format.

Bioinformatics analyses were performed on the High Performance Computing Facility takti CPU cluster at University of Maryland Baltimore County. Data quality was analyzed using FastQC v0.11.8 (available at: <http://bioinformatics.babraham.ac.uk/projects/fastqc/>). Ribosomal RNA were filtered using SortMeRNA v2.1b (60). Transcript-level abundance was quantified using the quasi-mapping-based mode in Salmon v1.0.0 (61), mapping to GRCm38 (mm10) mouse reference genome. Transcript-level abundance were aggregated to gene-level abundance using tximport (62), and DESeq2 (63) was used for differential expression analyses. PCA was performed using the mixOmics package (64). Tximport, DESeq2, and mixOmics packages were run in R v3.6.1 in RStudio v1.2. Pathway enrichment analysis were performed following the protocols described by Reimand *et al.* (65). Enriched biological pathways in each group were identified using g:Profiler (66) based on Gene Ontology biological process database. The biological pathway networks were built on the basis of the g:Profiler results using Cytoscape v3.8.0 (67). SLEA was performed as previously described at (<https://genomemedicine.biomedcentral.com/articles/10.1186/gm327>). Briefly, the mean expression of 10,000 random sets of genes the same size as the scored gene set were calculated as used as the null distribution for each sample. The mean expression of the scored gene set was then calculated and transformed to  $z$  score based on the null distribution (SLEA score). Gene sets were used from the Gene Ontology Biological Process database for phagocytosis (M16307), regulation of autophagy (M10281), and regulation of ROS biosynthetic process (M15379). DAM/senescence gene set was used from Hu *et al.* (68).

## Neurobehavioral testing

The following behavior tests were performed with mice and group information blinded to the operators. To minimize stress and fatigue, each test was performed on a different day.

### Motor function

**Rotarod.** Locomotor function and coordination were assessed using a rotarod as previously described (43, 69). The mouse was placed on a rotarod device (IITC Life Science Inc.), and their latency to falling off the accelerating rotarod was recorded. The acceleration settings for the device were 4 to 40 rpm over 90 s, with each trial lasting for a maximum of 300 s. Individual scores from three trials were averaged and evaluated relative to their baseline latencies.

**Grip strength.** Grip strength was measured using a digital grip strength meter (Bioseb BP, In Vivo Research Instruments, France) as previously described (43, 69). Forelimb grip strength was measured from the mouse using both the ipsilateral and contralateral forepaws together. The mouse was held by its tail, the forelimbs were placed on the grasping metal wire grid, and the mouse gripped the wire grid attached to the force transducer. Once the grip was secured, the animal was slowly pulled away from the bar. The maximal average force exerted on the grip strength meter by both forepaws was averaged from 10 trials per day for each mouse.

**Gait dynamics.** Analysis of gait and posture was performed with the CatWalk XT automated system as mentioned in our previous publications (Noldus) (42, 70). Acquisition of data took place in a darkened room with red light. The CatWalk apparatus records print position, gait postures, and weight distribution through its green illuminated walkway. A minimum of three valid runs, complete crossings with no turns or scaling of sidewalls, were obtained for each tested mouse. Runs that did not comply to the preset standards were excluded from the final analysis. The regularity index (%) expresses the number of normal step sequence patterns relative to the total number of paw placements. The regularity index is a fractional measure of interpaw coordination. In healthy, fully coordinated animals, its value is 100%. Stand (in seconds) is the duration of contact with the glass plate of the print. Stride length (in centimeters) is the distance (in distance units) between successive placements of the same paw. Swing speed (in centimeters per second) is the speed (in distance units per second) of the paw during swing (swing speed = stride length / swing). The body speed (in centimeters per second) of a step cycle of a specific paw is calculated by dividing the distance that the animal's body traveled from one initial contact of that paw to the next by the time to travel that distance. Step cycle (in seconds) is the time between two consecutive initial contacts of the same paw (step cycle = stand + swing).

### Cognitive function

**NOR task.** For testing nonhippocampal-mediated memory, mice in cohort 3 underwent NOR, as previously described (43, 71). Mice were tested in an open field apparatus after a 5-min habituation period on the first day. The time spent with two identical objects was recorded using ANY-maze software (Stoelting) on the second day of testing, and one of the familiar objects were switched out with a novel object on the third day. Testing stopped after each mouse went through a sum total of 30-s exploration time. Since mice would inherently prefer to explore novel objects, a preference for the novel object with an exploration time of more than 15 s was considered as having intact learning and memory skills.

**Y-maze test.** This task was used to assess the hippocampus-dependent spatial working memory of mice as previously described (55). The Y-maze (Stoelting, Wood Dale, IL) consisted of three identical arms: Each arm has 35 cm in length, 5 cm in width, and 10 cm in height, at an angle of 120° with respect to the other arms. One arm was randomly selected as the "start" arm, and the mouse was placed within and allowed to explore the maze freely for 5 min. Arm entries (arms A to C) were recorded by analyzing mouse activity using ANY-maze software (Stoelting). An arm entry was attributed when all four paws of the mouse entered the arm, and an alternation was designated when the mouse entered three different arms consecutively. The percentage of alternation was calculated as follows: total alternations  $\times$  100/(total arm entries – 2). If a mouse scored significantly greater than 50% alternations (the chance level for choosing the unfamiliar arm), then this was indicative of spatial working memory.

### Depressive-like behavior

**SR task.** SR test was performed for assessment of sociability function, as previously described (42, 55), using a three-chambered rectangular apparatus made of Plexiglas with each one at equal size (20 cm by 40 cm by 23 cm). An opening between the walls allows for free access to each chamber, which contains two identical wire mesh cup containers. Before testing, each mouse was single-housed overnight. On the first day, the tested mice were placed in the apparatus with two empty cups for a 10-min habituation period. On the second day, a stranger mouse was introduced and randomly placed inside one of the empty cups in either the left-side or right-side chamber, while the other cup was left empty. The tested mouse started from the middle chamber and allowed to freely explore all three chambers for an exploration period of 10 min. Afterward, a second unfamiliar stranger was placed inside the previously empty cup. The test subject was once again allowed to freely explore all three chambers for a period of 10 min. Exploration time that the subject mice spent with each cup versus stranger mouse was recorded using ANY-maze software (Stoelting). Since a socially functional mouse would naturally seek out unfamiliar mice for interaction, the test subject was considered capable of SR if index for novel mouse scored higher than 50%.

**TS test.** The TS test assesses depression-like behavior in mice and is based on the observation that mice develop an immobile posture when placed in an inescapable hemodynamic stress of being hung by their tail. The TS was performed as previously described (57, 72). Each mouse in cohort 3 was suspended at a height of 28 cm using 3M adhesive tape. The tip of the mouse tail was not wrapped around the rod while being suspended. The duration of immobility was recorded throughout the 5-min test period. The definition of immobility is passive hanging and complete motionlessness. Foam padding (7.62 cm in depth) was placed under the beam in case animals fall from the beam during the experiment.

**FS test.** FS testing is one of the most commonly used assays for the study of depressive-like behavior in rodents and was performed as previously described (42, 55). Mice were placed in transparent plastic cylinder (45 cm in height by 20 cm in diameter) filled with water (23°  $\pm$  2°C; 28 cm in depth) for 6 min. The duration of immobility was recorded using ANY-maze software (Stoelting).

### Multiplex ELISA

Cerebellar tissue and the cortex tissue surrounding the lesion area were excised. Tissues were loaded into tissue homogenizing tubes

(Bertin Corp.) on ice with 200  $\mu$ l of NP-40 cell lysis buffer supplemented with 1 $\times$  Halt protease and phosphatase inhibitor cocktail (Thermo Fisher Scientific) and then homogenized using a Fastprep FP120 homogenizer (Thermo Savant Bio 101) at 6.5 m/s in a 4°C cold room for 2 min, with 30 s of incubation on ice at 30-s intervals. Lysates were transferred into 1.5-ml centrifuge tubes and spun at 13,000 rpm for 10 min at 4°C. Cleared supernatant was collected, and protein concentration was quantified using Pierce bicinchoninic acid (BCA) protein assay kit (Thermo Fisher Scientific). Multiplex ELISA was performed on a Luminex FlexMAP 3D (Millipore Sigma) using a premixed 32-plex cytokine magnetic bead panel (MilliporeSigma) following the kit protocol. Undiluted cleared tissue lysate (25  $\mu$ l) was assayed in technical duplicates. Cytokine concentrations were determined by interpolation to known standard curves, followed by normalization to total protein concentration. Samples below the limit of detection were set to the lowest standard concentration. Analytes that were not within detectable limits or showed no change after injury are not shown.

### Lesion volume, neuronal counting, immunohistochemistry, and quantification

At 14 days after injury, mice were perfused intracardially with normal saline, followed by 4% paraformaldehyde solution. The brain was extracted and embedded in Tissue-Tek OCT compound (Sakura). Serial sections of 40- $\mu$ m thickness were placed on Superfrost Plus slides (Thermo Fisher Scientific). Every eighth section was selected for analysis beginning from the foremost section. Lesion volume was performed after staining with FD Cresyl Violet Solution (FD NeuroTechnologies Inc., catalog no. PS102-01). Quantification of the lesion volume was performed with the Stereoinvestigator software (MBF Biosciences) as previously described (55). By outlining the missing tissue on the injured hemisphere, the software was able to estimate lesion volume with the Cavalieri method at a grid spacing of 0.1 mm. For quantifications of neuronal cell loss post injury, the optical fractionator method of unbiased stereology was used in the Stereoinvestigator software as previously described (55, 57). In the dentate gyrus region of the hippocampus, every fourth section was analyzed for a total of eight sections per mouse, beginning at bregma  $-2.15$  mm and ending at  $-3.39$  mm. The number of surviving neurons in each field was divided by the volume of the region of interest to obtain the neuronal cells density expressed in cells per cubic millimeter

For immunohistochemistry (IHC), brain slices were washed three times with PBS, followed by blocking in 5% normal goat serum containing 0.3% Triton X-100 in PBS for 2 hours. The primary antibodies were added into blocking buffer and incubated with brain sections overnight at 4°C. Sections were rinsed with PBS three times and then incubated with secondary antibodies in blocking buffer for 2 hours at room temperature, followed by counterstaining with 4',6-diamidino-2-phenylindole (DAPI; catalog no. MBD0015, Sigma-Aldrich) for 10 min. After washing with PBS, sections were mounted onto glass slides with coverslips using an anti-fade Hydromount solution (National Diagnostics). The following primary and secondary antibodies were used: rabbit anti-Iba1 (1:1000; Wako, catalog no. 019-19741), rat anti-CD68 (1:1000; BioLegend, catalog no. 137002), Alexa Fluor 546 goat anti-rabbit immunoglobulin G (IgG; 1:800; Invitrogen), and Alexa Fluor 647 goat anti-rat IgG (1:800; Invitrogen). The green channel was left blank for imaging of AF.

Eight sections from each mouse in Veh/TBI and PLX5622/TBI groups were stained and imaged, and a total of  $N = 8$  mice per group were used in the analysis. Images were acquired using a Leica TCS SP5 II Tunable Spectral Confocal microscope system (Leica Microsystems). For each section, four cortex regions in the ipsilateral side close to the lesion core were imaged and four regions in the contralateral cortex by identical imaging parameters with three times zooming in under a 20 $\times$  lens. Using the NIH ImageJ software (1.53), a single view, an area of 258.84  $\mu$ m by 258.84  $\mu$ m with 512  $\times$  512 resolution, was formed by the z-axis projection of 10 layers covering the entire depth. The number of Iba1<sup>+</sup> cells, CD68<sup>+</sup> counts, or autofluorescence particles was quantified automatically by the "Analyze Particles" function in ImageJ after background subtraction and signal filtering. For each animal, the mean value of four regions on the same side was taken into statistical analysis. The signal colocalization of autofluorescence with Iba1 or CD68 was confirmed by the "Orthogonal View" function in ImageJ (43, 57). All IHC experiments were performed with appropriate positive control tissue and primary/secondary only negative controls. IHC analysis was performed by an investigator blinded to experimental groups.

### Postmortem human brain IHC

Human brain tissue for this study was obtained from the Department of Pathology and Laboratory Medicine at UT Health Science Center at Houston. Blocks of tissue were dissected from the brains of three deceased individuals (14-year-old female, 75-year-old male, and 97-year-old female). To be consistent with the animal study, the somatosensory and visual cortex were chosen to perform the microglia and autofluorescence analysis. Formalin-fixed paraffin-embedded sections were immunostained with Iba1 antibody using tyramide signal amplification method (Biotium). Briefly, after deparaffinization, the sections were blocked in 0.3% hydrogen peroxide and blocking buffer (1% bovine serum albumin with 0.5% Triton X-100 in PBS), serially, and then the sections were incubated with anti-human Iba1 mouse monoclonal antibody (1:200; FUJIFILM, catalog no. NCP27). The primary antibody was detected by horseradish peroxidase-conjugated goat anti-mouse secondary antibody (1:200) and colorized with CF488A tyramide dye in amplification buffer. Without autofluorescence elimination, the sections were coverslipped using Fluoroshield with DAPI mounting solution (Sigma-Aldrich). To obtain the representative images, the neocortex and subcortical white matter was scanned using a Leica THUNDER Imager DMi8 under 10 $\times$  lens, and the high-magnification images (63 $\times$  lens) were also taken from the same regions.

### Primary microglia cell cultures

Microglial cultures were prepared from the cerebral cortices of neonatal (1- to 2-day-old) C57BL/6 mice, as described in prior publication (73). Briefly, cortices were dissected from neonates in chilled ice-cold HBSS, dissociated with 0.25% trypsin-EDTA (Gibco, catalog no. 25200-056) and evenly distributed in poly-D-lysine-precoated T75 flasks. The mixed glial cells were grown in Dulbecco's modified Eagle's medium (DMEM)/F12 (Invitrogen, catalog no. 11320033) supplemented with 10% fetal bovine serum (Invitrogen, catalog no. 10082147) and 1% penicillin-streptomycin (Invitrogen, catalog no. 15140-122) at 37°C with 5% CO<sub>2</sub>. To induce microglia growth, recombinant murine granulocyte-macrophage CSF (50 ng/ml; Peprotech, catalog no. 315-03) was added after 48 hours of

culture. Once the cells had grown to confluence, the flasks were shaken at 100 rpm for 1 hour at 37°C to isolate microglia. Then, the isolated microglia were plated in 12-well plates and 8-well chamber slides for downstream experiments. On the day of experiment, microglia were pretreated with lipopolysaccharide (100 ng/ml; *Escherichia coli* O111:B4; Sigma-Aldrich, L2630) for 2 hours before addition of neural debris from slick mice.

### Preparation of feeder neurons for phagocytosis assay

On the day of experiment, transgenic SLICK mice were euthanized. Immediately after intracardial perfusion with ice-cold normal saline, a tissue punctum of the cerebral cortex was taken from the brain (tissue weight, 36 mg) and mechanically dissociated on a 70- $\mu$ m cell strainer. The tissue was spun down at 1500 rpm in 4°C before resuspension in 1 ml of RPMI 1640. For flow cytometry, a total volume of 100  $\mu$ l of the resuspended neural debris was added to each well, with the same volume of RPMI 1640 added to control groups. For ICC, 10  $\mu$ l of the resuspended tissue soup was added to each well. Plates were incubated at 37°C for 2 hours. After the incubation period with neural debris, we aspirated the remaining medium and rinsed all cells twice with prewarmed PBS before downstream experiments.

### Immunocytochemistry

Microglia were fixed for 20 min with 4% paraformaldehyde in 0.1 M PBS after treatment with neural debris. The cells were rinsed with PBS and incubated sequentially in: (i) blocking solution (PBS containing 5% normal goat serum and 0.1% Triton X-100), (ii) primary antibodies [MAP2 (1:1000; BioLegend, catalog no. 801801), myelin CNPase (1:1000; BioLegend, catalog no. 836404), and Iba-1 (1:500; Cell Signaling Technology, catalog no.17198S)], (iii) PBS, (iv) secondary antibody(ies) [goat anti-mouse Alexa Fluor 546 (1:1000; Invitrogen, catalog no. A11030) and goat anti-rabbit Alexa Fluor 633 (1:1000; Invitrogen, catalog no. A21071)], and (v) DAPI nuclei marker (1:1000; Sigma-Aldrich). Chamber slides were examined with a Leica confocal microscope.

### Flow cytometry of cultured microglia

The microglia were dissociated with trypsin and collected with completed DMEM. Cells were centrifuged at 1500 rpm and resuspended in FACS buffer before being moved to 5 ml of FACS tubes for staining. Microglia cells were incubated in blocking buffer (CD16/32-APC; 1:100; BioLegend) on ice for 10 min to block Fc receptor. Surface antibody cocktails were prepared with CD45/PerCP-Cy5.5 (1:100; BioLegend) and CD11b/APC-Fire 750 (1:100; BioLegend) including viability dye Zombie Aqua. Intracellular staining was performed with MAP2/Alexa Fluor 594 (1:100) and myelin CNPase/Alexa Fluor 647 (1:100).

### Statistical analysis

Data from individual experiments are presented as means  $\pm$  SEM. Nonparametric data were analyzed by Mann-Whitney test. One-way analysis of variance (ANOVA) was used with Tukey's multiple comparisons test, and group effects were determined by two-way ANOVA analysis with Sidak's or Tukey's post hoc correction for multiple comparisons. Behavioral data were analyzed by two-way repeated measures ANOVA. All behavioral, histological and ex vivo studies were performed by an investigator blinded to genotype, treatment, and surgical condition. Statistical analysis was performed

using GraphPad Prism software v. 9.0 (GraphPad Software, Inc., La Jolla, CA).  $P \leq 0.05$  was considered statistically significant.

### Supplementary Materials

This PDF file includes:

Figs. S1 to S16

Table S1

[View/request a protocol for this paper from Bio-protocol.](#)

### REFERENCES AND NOTES

1. D. M. Angelova, D. R. Brown, Microglia and the aging brain: Are senescent microglia the key to neurodegeneration? *J. Neurochem.* **151**, 676–688 (2019).
2. B. Spittau, Aging microglia-phenotypes, functions and implications for age-related neurodegenerative diseases. *Front. Aging Neurosci.* **9**, 194 (2017).
3. W. T. Wong, Microglial aging in the healthy CNS: Phenotypes, drivers, and rejuvenation. *Front. Cell. Neurosci.* **7**, 22 (2013).
4. H. Nakanishi, Z. Wu, Microglia-aging: Roles of microglial lysosome- and mitochondria-derived reactive oxygen species in brain aging. *Behav. Brain Res.* **201**, 1–7 (2009).
5. T. Jung, N. Bader, T. Grune, Lipofuscin: Formation, distribution, and metabolic consequences. *Ann. N. Y. Acad. Sci.* **1119**, 97–111 (2007).
6. X. Hu, B. Xu, W. Ge, The role of lipid bodies in the microglial aging process and related diseases. *Neurochem. Res.* **42**, 3140–3148 (2017).
7. A. Moreno-García, A. Kun, O. Calero, M. Medina, M. Calero, An overview of the role of lipofuscin in age-related neurodegeneration. *Front. Neurosci.* **12**, 464 (2018).
8. B. C. Farmer, A. E. Walsh, J. C. Klumper, L. A. Johnson, Lipid droplets in neurodegenerative disorders. *Front. Neurosci.* **14**, 742 (2020).
9. P. Fuger, J. K. Hefendehl, K. Veeraghavalu, A. C. Wendeln, C. Schlosser, U. Obermüller, B. M. Wegenast-Braun, J. J. Neher, P. Martus, S. Kohsaka, M. Thunemann, R. Feil, S. S. Sisodia, A. Skodras, M. Jucker, Microglia turnover with aging and in an Alzheimer's model via long-term in vivo single-cell imaging. *Nat. Neurosci.* **20**, 1371–1376 (2017).
10. A. R. Najafi, J. Craspe, S. Jiang, W. Ng, A. Mortazavi, B. L. West, K. N. Green, A limited capacity for microglial repopulation in the adult brain. *Glia* **66**, 2385–2396 (2018).
11. Z. Si, L. Sun, X. Wang, Evidence and perspectives of cell senescence in neurodegenerative diseases. *Biomed. Pharmacother.* **137**, 111327 (2021).
12. P. Y. Ng, T. L. McNeely, D. J. Baker, Untangling senescent and damage-associated microglia in the aging and diseased brain. *FEBS J.*, 10.1111/febs.16315 (2021).
13. S. Singh Kushwaha, N. Patro, I. Kumar Patro, A sequential study of age-related lipofuscin accumulation in hippocampus and striate cortex of rats. *Ann. Neurosci.* **25**, 223–233 (2019).
14. S. F. Yanuck, Microglial phagocytosis of neurons: Diminishing neuronal loss in traumatic, infectious, inflammatory, and autoimmune CNS disorders. *Front. Psych.* **10**, 712 (2019).
15. D. A. Galloway, A. E. M. Phillips, D. R. J. Owen, C. S. Moore, Phagocytosis in the brain: Homeostasis and disease. *Front. Immunol.* **10**, 790 (2019).
16. E. C. Koellhoffer, L. D. McCullough, R. M. Ritzel, Old maids: Aging and its impact on microglia function. *Int. J. Mol. Sci.* **18**, 769 (2017).
17. J. C. Burns, B. Coteleur, D. M. Walther, B. Bajrami, S. J. Rubino, R. Wei, N. Franchimont, S. L. Cotman, R. M. Ransohoff, M. Mingueneau, Differential accumulation of storage bodies with aging defines discrete subsets of microglia in the healthy brain. *eLife* **9**, e57495 (2020).
18. D. J. Weatherall, D. R. Higgs, J. B. Clegg, The molecular pathology of the alpha globin genes. *Br. J. Cancer Suppl.* **9**, 17–22 (1988).
19. A. M. Di Battista, N. M. Heinsinger, G. W. Rebeck, Alzheimer's disease genetic risk factor APOE $\epsilon$ 4 also affects normal brain function. *Curr. Alzheimer Res.* **13**, 1200–1207 (2016).
20. U. T. Brunk, A. Terman, Lipofuscin: Mechanisms of age-related accumulation and influence on cell function. *Free Radic. Biol. Med.* **33**, 611–619 (2002).
21. S. M. O'Neil, K. G. Witcher, D. B. McKim, J. P. Godbout, Forced turnover of aged microglia induces an intermediate phenotype but does not rebalance CNS environmental cues driving priming to immune challenge. *Acta Neuropathol. Commun.* **6**, 129 (2018).
22. S. Whelan, E. Ophir, M. F. Kotturi, O. Levy, S. Ganguly, L. Leung, I. Vaknin, S. Kumar, L. Dassa, K. Hansen, D. Bernados, B. Murter, A. Soni, J. M. Taube, A. N. Fader, T. L. Wang, I. M. Shih, M. White, D. M. Pardoll, S. C. Liang, PVRI and PVRL2 are induced in cancer and inhibit CD8<sup>+</sup> T-cell function. *Cancer Immunol. Res.* **7**, 257–268 (2019).
23. G. Novikova, M. Kapoor, J. Tcw, E. M. Abud, A. G. Efthymiou, S. X. Chen, H. Cheng, J. F. Fullard, J. Bendl, Y. Liu, P. Roussos, J. L. Bjorkegren, Y. Liu, W. W. Poon, K. Hao, E. Marcora,

- A. M. Goate, Integration of Alzheimer's disease genetics and myeloid genomics identifies disease risk regulatory elements and genes. *Nat. Commun.* **12**, 1610 (2021).
24. B. Fu, S. Yin, X. Lin, L. Shi, Y. Wang, S. Zhang, Q. Zhao, Z. Li, Y. Yang, H. Wu, PTPN14 aggravates inflammation through promoting proteasomal degradation of SOCS7 in acute liver failure. *Cell Death Disease* **11**, 803 (2020).
  25. B. Karaahmet, L. Le, M. S. Mendes, A. K. Majewska, M. K. O'Banion, Repopulated microglia under expression of Cxcl13 with differential changes in Tau phosphorylation but do not impact amyloid pathology. *J. Neuroinflammation* **19**, 173 (2022).
  26. S. Rangaraju, E. B. Dammer, S. A. Raza, P. Rathakrishnan, H. Xiao, T. Gao, D. M. Duong, M. W. Pennington, J. J. Lah, N. T. Seyfried, A. I. Levey, Identification and therapeutic modulation of a pro-inflammatory subset of disease-associated-microglia in Alzheimer's disease. *Mol. Neurodegener.* **13**, 24 (2018).
  27. M. Lalancette-Hebert, V. Swarup, J. M. Beaulieu, I. Bohacek, E. Abdelhamid, Y. C. Weng, S. Sato, J. Kriz, Galectin-3 is required for resident microglia activation and proliferation in response to ischemic injury. *J. Neurosci.* **32**, 10383–10395 (2012).
  28. B. J. Lerman, E. P. Hoffman, M. L. Sutherland, K. Bouri, D. K. Hsu, F. T. Liu, J. D. Rothstein, S. M. Knoblach, Deletion of galectin-3 exacerbates microglial activation and accelerates disease progression and demise in a SOD1(G93A) mouse model of amyotrophic lateral sclerosis. *Brain Behav.* **2**, 563–575 (2012).
  29. M. R. P. Elmore, L. A. Hohsfield, E. A. Kramar, L. Soreq, R. J. Lee, S. T. Pham, A. R. Najafi, E. E. Spangenberg, M. A. Wood, B. L. West, K. N. Green, Replacement of microglia in the aged brain reverses cognitive, synaptic, and neuronal deficits in mice. *Aging Cell* **17**, e12832 (2018).
  30. J. He, R. M. Ritzel, J. Wu, Functions and mechanisms of the voltage-gated proton channel Hv1 in brain and spinal cord injury. *Front. Cell. Neurosci.* **15**, 662971 (2021).
  31. J. Marschallinger, T. Iram, M. Zardeneta, S. E. Lee, B. Lehallier, M. S. Haney, J. V. Pluvinaige, V. Mathur, O. Hahn, D. W. Morgens, J. Kim, J. Tevini, T. K. Felder, H. Wolinski, C. R. Bertozzi, M. C. Bassik, L. Aigner, T. Wyss-Coray, Lipid-droplet-accumulating microglia represent a dysfunctional and proinflammatory state in the aging brain. *Nat. Neurosci.* **23**, 194–208 (2020).
  32. M. Candlish, J. K. Hefendehl, Microglia phenotypes converge in aging and neurodegenerative disease. *Front. Neurol.* **12**, 660720 (2021).
  33. M. K. Shimabukuro, L. G. Langhi, I. Cordeiro, J. M. Brito, C. M. Batista, M. P. Mattson, V. Mello Coelho, Lipid-laden cells differentially distributed in the aging brain are functionally active and correspond to distinct phenotypes. *Sci. Rep.* **6**, 23795 (2016).
  34. W. J. Streit, Q. S. Xue, J. Tischer, I. Bechmann, Microglial pathology. *Acta Neuropathol. Commun.* **2**, 142 (2014).
  35. P. Gomez-Ramos, M. Asuncion Moran, Ultrastructural localization of intraneuronal A $\beta$ -peptide in Alzheimer disease brains. *J. Alzheimers Dis.* **11**, 53–59 (2007).
  36. B. T. Casali, K. P. MacPherson, E. G. Reed-Geaghan, G. E. Landreth, Microglia depletion rapidly and reversibly alters amyloid pathology by modification of plaque compaction and morphologies. *Neurobiol. Dis.* **142**, 104956 (2020).
  37. C. C. Liu, C. C. Liu, T. Kanekiyo, H. Xu, G. Bu, Apolipoprotein E and Alzheimer disease: Risk, mechanisms and therapy. *Nat. Rev. Neurol.* **9**, 106–118 (2013).
  38. C. G. Fernandez, M. E. Hamby, M. L. McReynolds, W. J. Ray, The role of APOE4 in disrupting the homeostatic functions of astrocytes and microglia in aging and Alzheimer's disease. *Front. Aging Neurosci.* **11**, 14 (2019).
  39. G. Sienski, P. Narayan, J. M. Bonner, N. Kory, S. Boland, A. A. Arczewska, W. T. Ralvenius, L. Akay, E. Lockshin, L. He, B. Milo, A. Graziosi, V. Baru, C. A. Lewis, M. Kellis, D. M. Sabatini, L. H. Tsai, S. Lindquist, APOE4 disrupts intracellular lipid homeostasis in human iPSC-derived glia. *Sci. Transl. Med.* **13**, eaaz4564 (2021).
  40. M. D. Cusimano, O. Saarela, K. Hart, S. Zhang, S. R. McFaul, A population-based study of fall-related traumatic brain injury identified in older adults in hospital emergency departments. *Neurosurg. Focus* **49**, E20 (2020).
  41. D. J. Loane, A. Kumar, B. A. Stoica, R. Cabatbat, A. I. Faden, Progressive neurodegeneration after experimental brain trauma: Association with chronic microglial activation. *J. Neuropathol. Exp. Neurol.* **73**, 14–29 (2014).
  42. R. M. Ritzel, Y. Li, J. He, N. Khan, S. J. Doran, A. I. Faden, J. Wu, Sustained neuronal and microglial alterations are associated with diverse neurobehavioral dysfunction long after experimental brain injury. *Neurobiol. Dis.* **136**, 104713 (2020).
  43. R. M. Ritzel, Y. Li, Z. Lei, J. Carter, J. He, H. M. C. Choi, N. Khan, H. Li, S. Allen, M. M. Lipinski, A. I. Faden, J. Wu, Functional and transcriptional profiling of microglial activation during the chronic phase of TBI identifies an age-related driver of poor outcome in old mice. *Geroscience* **44**, 1407–1440 (2022).
  44. S. E. Marsh, A. J. Walker, T. Kamath, L. Dissing-Olesen, T. R. Hammond, T. Y. de Soysa, A. M. H. Young, S. Murphy, A. Abdullaouf, N. Nadaf, C. Dufort, A. C. Walker, L. E. Lucca, V. Kozareva, C. Vanderburg, S. Hong, H. Bulstrode, P. J. Hutchinson, D. J. Gaffney, D. A. Hafler, R. J. M. Franklin, E. Z. Macosko, B. Stevens, Dissection of artifactual and confounding glial signatures by single-cell sequencing of mouse and human brain. *Nat. Neurosci.* **25**, 306–316 (2022).
  45. J. T. Park, Y. S. Lee, K. A. Cho, S. C. Park, Adjustment of the lysosomal-mitochondrial axis for control of cellular senescence. *Ageing Res. Rev.* **47**, 176–182 (2018).
  46. C. Vida, I. M. de Toda, J. Cruces, A. Garrido, M. Gonzalez-Sanchez, M. De la Fuente, Role of macrophages in age-related oxidative stress and lipofuscin accumulation in mice. *Redox Biol.* **12**, 423–437 (2017).
  47. J. Konig, C. Ott, M. Hugo, T. Jung, A. L. Bulteau, T. Grune, A. Hohn, Mitochondrial contribution to lipofuscin formation. *Redox Biol.* **11**, 673–681 (2017).
  48. V. Martinez-Cisuelo, J. Gomez, I. Garcia-Junceda, A. Naudi, R. Cabre, N. Mota-Martorell, M. Lopez-Torres, M. Gonzalez-Sanchez, R. Pamplona, G. Barja, Rapamycin reverses age-related increases in mitochondrial ROS production at complex I, oxidative stress, accumulation of mtDNA fragments inside nuclear DNA, and lipofuscin level, and increases autophagy, in the liver of middle-aged mice. *Exp. Gerontol.* **83**, 130–138 (2016).
  49. L. Li, J. Tan, Y. Miao, P. Lei, Q. Zhang, ROS and autophagy: Interactions and molecular regulatory mechanisms. *Cell. Mol. Neurobiol.* **35**, 615–621 (2015).
  50. M. W. Ma, J. Wang, K. M. Dhandapani, R. Wang, D. W. Brann, NADPH oxidases in traumatic brain injury - Promising therapeutic targets? *Redox Biol.* **16**, 285–293 (2018).
  51. D. W. Simon, M. J. McGeachy, H. Bayir, R. S. B. Clark, D. J. Loane, P. M. Kochanek, The far-reaching scope of neuroinflammation after traumatic brain injury. *Nat. Rev. Neurol.* **13**, 572 (2017).
  52. J. Wu, M. M. Lipinski, Autophagy in neurotrauma: Good, bad, or dysregulated. *Cell* **8**, 693 (2019).
  53. J. P. Barrett, R. J. Henry, S. Villapol, B. A. Stoica, A. Kumar, M. P. Burns, A. I. Faden, D. J. Loane, NOX2 deficiency alters macrophage phenotype through an IL-10/STAT3 dependent mechanism: Implications for traumatic brain injury. *J. Neuroinflammation* **14**, 65 (2017).
  54. A. Kumar, J. P. Barrett, D. M. Alvarez-Croda, B. A. Stoica, A. I. Faden, D. J. Loane, NOX2 drives M1-like microglial/macrophage activation and neurodegeneration following experimental traumatic brain injury. *Brain Behav. Immun.* **58**, 291–309 (2016).
  55. R. M. Ritzel, J. He, Y. Li, T. Cao, N. Khan, B. Shim, B. Sabirzhanov, T. Aubrecht, B. A. Stoica, A. I. Faden, L. J. Wu, J. Wu, Proton extrusion during oxidative burst in microglia exacerbates pathological acidosis following traumatic brain injury. *Glia* **69**, 746–764 (2021).
  56. E. Spangenberg, P. L. Severson, L. A. Hohsfield, J. Crapser, J. Zhang, E. A. Burton, Y. Zhang, W. Spevak, J. Lin, N. Y. Phan, G. Habets, A. Rymar, G. Tsang, J. Walters, M. Nespi, P. Singh, S. Broome, P. Ibrahim, C. Zhang, G. Bollag, B. L. West, K. N. Green, Sustained microglial depletion with CSF1R inhibitor impairs parenchymal plaque development in an Alzheimer's disease model. *Nat. Commun.* **10**, 3758 (2019).
  57. Y. Li, R. M. Ritzel, N. Khan, T. Cao, J. He, Z. Lei, J. J. Matyas, B. Sabirzhanov, S. Liu, H. Li, B. A. Stoica, D. J. Loane, A. I. Faden, J. Wu, Delayed microglial depletion after spinal cord injury reduces chronic inflammation and neurodegeneration in the brain and improves neurological recovery in male mice. *Theranostics* **10**, 11376–11403 (2020).
  58. F. Lei, N. Cui, C. Zhou, J. Chodosh, D. G. Vavvas, E. I. Paschalis, CSF1R inhibition by a small-molecule inhibitor is not microglia specific; affecting hematopoiesis and the function of macrophages. *Proc. Natl. Acad. Sci. U.S.A.* **117**, 23336–23338 (2020).
  59. R. M. Ritzel, Y. J. Lai, J. D. Crapser, A. R. Patel, A. Schreengost, J. M. Grenier, N. S. Mancini, A. Patrizz, E. R. Jellison, D. Morales-Scheihing, V. R. Venna, J. K. Kofler, F. Liu, R. Verma, L. D. McCullough, Aging alters the immunological response to ischemic stroke. *Acta Neuropathol.* **136**, 89–110 (2018).
  60. E. Kopylova, L. Noe, H. Touzet, SortMeRNA: Fast and accurate filtering of ribosomal RNAs in metatranscriptomic data. *Bioinformatics* **28**, 3211–3217 (2012).
  61. R. Patro, G. Duggal, M. I. Love, R. A. Irizarry, C. Kingsford, Salmon provides fast and bias-aware quantification of transcript expression. *Nat. Methods* **14**, 417–419 (2017).
  62. C. Soneson, M. I. Love, M. D. Robinson, Differential analyses for RNA-seq: Transcript-level estimates improve gene-level inferences. *F1000Res* **4**, 1521 (2015).
  63. M. I. Love, W. Huber, S. Anders, Moderated estimation of fold change and dispersion for RNA-seq data with DESeq2. *Genome Biol.* **15**, 550 (2014).
  64. F. Rohart, B. Gautier, A. Singh, K. A. Le, mixOmics: An R package for 'omics feature selection and multiple data integration. *PLOS Comput. Biol.* **13**, e1005752 (2017).
  65. J. Reimand, R. Isserlin, V. Voisin, M. Kucera, C. Tannus-Lopes, A. Rostamianfar, L. Wadi, M. Meyer, J. Wong, C. Xu, D. Merico, G. D. Bader, Pathway enrichment analysis and visualization of omics data using g:Profiler, GSEA, Cytoscape and EnrichmentMap. *Nat. Protoc.* **14**, 482–517 (2019).
  66. U. Raudvere, L. Kolberg, I. Kuzmin, T. Arak, P. Adler, H. Peterson, J. Vilo, g:Profiler: A web server for functional enrichment analysis and conversions of gene lists (2019 update). *Nucleic Acids Res.* **47**, W191–W198 (2019).
  67. P. Shannon, A. Markiel, O. Ozier, N. S. Baliga, J. T. Wang, D. Ramage, N. Amin, B. Schwikowski, T. Ideker, Cytoscape: A software environment for integrated models of biomolecular interaction networks. *Genome Res.* **13**, 2498–2504 (2003).

68. Y. Hu, G. L. Fryatt, M. Ghorbani, J. Obst, D. A. Menassa, M. Martin-Estebane, T. A. O. Muntslag, A. Olmos-Alonso, M. Guerrero-Carrasco, D. Thomas, M. S. Cragg, D. Gomez-Nicola, Replicative senescence dictates the emergence of disease-associated microglia and contributes to A $\beta$  pathology. *Cell Rep.* **35**, 109228 (2021).
69. S. J. Doran, R. M. Ritzel, E. P. Glaser, R. J. Henry, A. I. Faden, D. J. Loane, Sex differences in acute neuroinflammation after experimental traumatic brain injury are mediated by infiltrating myeloid cells. *J. Neurotrauma* **36**, 1040–1053 (2019).
70. J. J. Matyas, C. M. O'Driscoll, L. Yu, M. Coll-Miro, S. Daugherty, C. L. Renn, A. I. Faden, S. G. Dorsey, J. Wu, Truncated TrkB.T1-mediated astrocyte dysfunction contributes to impaired motor function and neuropathic pain after spinal cord injury. *J. Neurosci.* **37**, 3956–3971 (2017).
71. Y. Li, R. M. Ritzel, Z. Lei, T. Cao, J. He, A. I. Faden, J. Wu, Sexual dimorphism in neurological function after SCI is associated with disrupted neuroinflammation in both injured spinal cord and brain. *Brain Behav. Immun.* **101**, 1–22 (2022).
72. J. Wu, Z. Zhao, A. Kumar, M. M. Lipinski, D. J. Loane, B. A. Stoica, A. I. Faden, Endoplasmic reticulum stress and disrupted neurogenesis in the brain are associated with cognitive impairment and depressive-like behavior after spinal cord injury. *J. Neurotrauma* **33**, 1919–1935 (2016).
73. B. Sabirzhanov, J. Matyas, M. Coll-Miro, L. L. Yu, A. I. Faden, B. A. Stoica, J. Wu, Inhibition of microRNA-711 limits angiotensin-1 and Akt changes, tissue damage, and motor dysfunction after contusive spinal cord injury in mice. *Cell Death Dis.* **10**, 839 (2019).

**Acknowledgments:** We thank Plexxikon Inc. for the use of PLX5622 and L. J. Wu at Mayo Clinic for the use of Hv1 KO mice. We thank J. Faden, V. Meadows, J. Carter, H. Li, and W. Shoap for assistance with animal care and behavioral experiments. We would also like to thank E. Glaser, N. Braganca, N. Hegdekar, N. Khan, and C. Colson for assistance with flow cytometry experiments. We appreciate the advice of E. Jellison, Associate Professor of Immunology and

Director of the Flow Cytometry Core at UCONN Health, Farmington, Connecticut. Last, we thank L. McCullough, Professor of Neurology at the University of Texas Health Science Center at Houston for providing support for our postmortem human brain study. **Funding:** This work was supported by grants from the NIH [K99NS116032 (to R.M.R.), RF1NS110637 (to J.W.), 2RF1NS094527 (to J.W.), R01NS110635 (to A.I.F. and J.W.), R01NS110825 (to J.W.), R01AG077541 (to J.W. and S.L.), and RF1AG069196 (to S.L.)] and Science Foundation Ireland (SFI 17/FRL/4860 to D.J.L.). **Author contributions:** R.M.R. conceived this study, designed and conducted most of the experiments, supervised the project, and wrote the manuscript. Y.L. performed the behavioral experiments. R.M.R., Y.L., and S.J.D. performed the flow cytometry experiments. Z.L. performed the IHC analysis. Y.L. and R.A.S. performed the histological analysis. J.H. and R.J.H. performed the animal surgeries. Y.J. and G.S. analyzed the RNA-seq data. R.K. and C.T. performed the immunostaining of postmortem human brain tissue. Y.J. performed the multiplex ELISA. G.S., S.L., A.I.F., and B.A.S. provided the feedback on the manuscript. J.W. and D.J.L. contributed to study conception and design and revised the manuscript. All authors have critically read and commented on the final paper. **Competing interests:** The authors declare that they have no competing interests. **Data and materials availability:** All data needed to evaluate the conclusions in the paper are present in the paper and/or the Supplementary Materials. All RNA-seq data were deposited in the Gene Expression Omnibus (GEO) under the accession number: GSE206618 (<https://ncbi.nlm.nih.gov/geo/query/acc.cgi?acc=GSE206618>). Source data are provided with this paper and have been archived at Zenodo (<https://zenodo.org/record/7295489#.Y2f-8OzML0M>).

Submitted 20 May 2022

Accepted 2 February 2023

Published 8 March 2023

10.1126/sciadv.add1101